

PFC/JA-90-14

MACROCLUMP MODEL OF THE NONLINEAR EVOLUTION OF THE
SIDE BAND INSTABILITY IN A HELICAL WIGGLER
FREE ELECTRON LASER

T.-Y. Brian Yang
Ronald C. Davidson

May, 1990

Plasma Fusion Center
Massachusetts Institute of Technology
Cambridge, MA 02139

Research was supported in part by the National Science Foundation, the Department of Energy High Energy Physics Division, the Naval Research Laboratory Plasma Physics Division and the Office of Naval Research.

Macroclump Model of the Nonlinear Evolution of the Sideband Instability in a Helical Wiggler Free Electron Laser

T.-Y. Brian Yang and Ronald C. Davidson
Plasma Fusion Center
Massachusetts Institute of Technology
Cambridge, Massachusetts 02139

ABSTRACT

The nonlinear evolution of a helical wiggler free electron laser is investigated within the framework of a macroclump model for the trapped electrons. The model describes the nonlinear evolution of a right-circularly polarized electromagnetic wave with frequency ω_s and wavenumber k_s , and slowly varying amplitude $\hat{a}_s(z, t)$ and phase $\delta_s(z, t)$ (eikonal approximation). The model further assumes that the trapped electrons can be treated as tightly bunched macroclumps that interact coherently with the radiation field. The analysis is carried out in the ponderomotive frame, which leads to a substantial simplification in both the analytical and numerical studies. As a first application, the nonlinear evolution of the primary signal is examined when $\partial/\partial l' = 0$ (no spatial variation of the wave amplitude and phase). The evolution equations are reduced to quadrature, and the maximum excursion of the wave amplitude $\hat{a}_{s, \max}$ is calculated analytically. Subsequently, the nonlinear evolution of the sideband instability is investigated, making use of the equations describing the self-consistent evolution of the wave amplitude \hat{a}_s and phase δ_s , which vary slowly with both space and time, together with the macroclump orbit equation. In the present analysis, the sideband signals are treated as perturbations (not necessarily small) about a constant-amplitude ($\hat{a}_s^0 = \text{const}$) primary electromagnetic wave with slowly varying phase $\delta_s^0(z')$. The coupled orbit and field equations are investigated analytically and numerically over a wide range of system parameters to determine detailed scaling properties of the sideband instability. The results of the present analysis suggest that free electron lasers operating with system parameters corresponding to the strong-pump regime [$(\Omega'_B/\Gamma'_0)^6/4 \gg 1$] are least vulnerable to the sideband instability. Moreover, the nonlinear evolution of the sideband instability is investigated numerically for system parameters corresponding to the Los Alamos free electron laser experiment. In several aspects, the numerical results are found to be in good qualitative agreement with the experimental results.

I. Introduction

There is growing experimental¹⁻²⁰ and theoretical²¹⁻⁷³ evidence that free-electron lasers (FEL's)⁷⁴⁻⁸⁰ are effective sources of coherent radiation generation by intense relativistic electron beams. Recent theoretical studies have included investigations of nonlinear effects²¹⁻⁴⁹ and saturation mechanisms, the influence of finite radial geometry on linear stability properties,⁵⁰⁻⁵⁵ novel magnetic field geometries for radiation generation,^{50,56-60} and fundamental studies of stability behavior.⁶¹⁻⁷² Since it is often desirable to operate an FEL as a high power radiation source in the high gain regime, the nonlinear effects²¹⁻⁴⁹ and saturation mechanisms are of considerable practical interest. In circumstance where a sufficiently broad spectrum of waves is excited, a quasilinear model has been developed by Dimos and Davidson²⁹ to describe the nonlinear evolution and saturation of the free electron laser instability. On the other hand, when the spectrum of the excited signal wave is relatively narrow, a simple trapping argument⁷⁵ has been used to estimate the saturation level. Another topic of considerable practical importance is the sideband instability^{5-8,21-23,39-49} which results from the bounce motion of electrons trapped in the (finite-amplitude) ponderomotive potential. It was first predicted theoretically by Kroll, Morton and Rosenbluth³⁹ that the bounce motion of the trapped electrons can lead to the unstable development of sideband signals. Numerical simulations⁴⁰⁻⁴⁹ and experimental observations⁵⁻⁸ subsequently demonstrated that sideband signals can grow to a significant level. In analytical investigations of the sideband instability, both kinetic^{21-23,84} and single-particle^{24,25,39} models have been developed. Making use of the Vlasov-Maxwell equations in the ponderomotive frame, Davidson²¹ investigated the sideband instability for perturbations about a self-consistent kinetic equilibrium state. In circumstances where the trapped electrons are localized near the bottom of the ponderomotive potential, it was found that the detailed stability properties are relatively insensitive to the form of the distribution of trapped electrons. In a subsequent analysis,²² the detailed dependence of the sideband instability on system parameters was examined. Moreover, Davidson and Wurtele²⁴ have developed a single-particle model (with appropriate statistical averages) to analyze the sideband instability in the ponderomotive frame. The effects of the untrapped electrons have also been con-

sidered.²⁵ Riyopoulos and Tang²⁶ recently developed a kinetic model to study the sideband instability for general distribution of trapped electrons. The influence of the sideband signal on the electron dynamics has also been investigated.²⁷ Furthermore, Sharp and Yu²⁸ have developed a kinetic model of the sideband instability in which the transverse variations of the wave fields are calculated self-consistently from Maxwell's equations. Recent studies of the sideband instability have also included a self-consistent one-dimensional kinetic analysis by Yang and Davidson⁸⁴ in which the detailed influence of the trapped-electron distribution on the sideband instability is determined.

Due to the complicated evolution of the electron distribution, most studies of nonlinear FEL behavior rely on numerical simulations. For the sideband instability, which involves both spatial and temporal variations, many periods of the ponderomotive potential need to be included. Consequently, the CPU time required in numerical simulations can be very long. In this paper, we present a simplified nonlinear model of the sideband instability in which all of the beam electrons are trapped in the ponderomotive potential. Furthermore, the trapped electrons are assumed to be tightly bunched into coherent macroclumps. Although, the "macroclump" model is idealized, the field evolution and the nonlinear motion of the macroclumps are determined self-consistently [Eqs. (40), (41) and (43)] within the model. Moreover, within the framework of the macroclump model, several analytical results are accessible, and the numerical analysis can be carried out in a straightforward manner to determine the nonlinear evolution of the system.

The present analysis is carried out in the ponderomotive frame, which leads to considerable simplification in the orbit equations [Eqs. (14) and (15)] and in the detailed investigation of the sideband instability.^{21-23,73,74,84} Moreover, the model has a conservation relation [Eq. (20)] which, when transformed to the laboratory frame, corresponds to energy conservation.

The theoretical model and assumptions are described in Sec. II. A tenuous, relativistic electron beam propagates through a constant-amplitude helical wiggler magnetic field with wavelength $\lambda_w = 2\pi/k_0 = \text{const}$, and normalized amplitude $a_w = e\hat{B}_w/mc^2k_0 = \text{const}$ [Eq. (1)]. The model neglects longitudinal perturba-

tions (Compton-regime approximation with $\delta\phi \simeq 0$) and transverse spatial variations ($\partial/\partial x = 0 = \partial/\partial y$). Moreover, the analysis is carried out for the case of a finite-amplitude primary electromagnetic wave (ω_s, k_s) with circular polarization and slowly varying normalized amplitude $\hat{a}_s(z, t)$ and wave phase $\delta(z, t)$ in the eikonal approximation [Eq. (2)]. A detailed investigation of the sideband instability simplifies considerably if the analysis is carried out in the ponderomotive frame^{21–23,73,74,84} moving with axial velocity $v_p = \omega_s/(k_s + k_0)$. In the ponderomotive frame (“primed” variables), the nonlinear evolution of $\hat{a}_s(z', t')$ and $\delta'_s(z', t')$ is described by Eqs. (5) and (6), and the electron orbits evolve according to Eq. (14). A conservation relation [Eq. (20)] associated with the self-consistent evolution of the electromagnetic field and the electron motion is readily derived from Eqs. (5) and (14). It is shown in Sec. II B that the conservation relation in Eq. (20) implies energy conservation [Eqs. (31) and (38)] in the laboratory frame. In Sec. II C, the macroclump model is introduced. In this model, all of the beam electrons are trapped in the ponderomotive potential. Furthermore, the trapped electrons are assumed to be tightly bunched into coherent macroclumps. The nonlinear evolution equations (5) and (6) for the amplitude and the phase of the electromagnetic wave are thereby simplified and reduce to Eqs. (40) and (41).

In Sec. III, the nonlinear evolution of the primary signal when $\partial/\partial l' = 0$ (no spatial variation in wave amplitude and phase) is investigated within the framework of the macroclump model. The assumption $\partial/\partial l' = 0$ readily reduces the evolution equations (40), (41) and (43) to the ordinary differential equations (46)-(48), which can be further reduced to quadrature [Eq. (60)]. Assuming $A_{s,0} = 0$ and $\theta'_{s,0} = 0$ in Eq. (62), the maximum amplitude excursion $A_{s,\max}$ is calculated analytically from Eq. (60). Except for a constant scale factor of order unity, the maximum amplitude so obtained is the same as the estimate of the nonlinear saturation amplitude obtained in the high-gain Compton regime⁷⁵ using a simple trapping argument.

The basic framework for studying the sideband instability is established in Sec. IV. In Sec. IV A, the self-consistent quasi-steady equilibrium state is described by Eqs. (68) and (69). The evolution equations (77)-(79) for the sideband signals, which are treated as perturbations about the quasi-steady equilibrium state, are derived in Sec. IV B.

In deriving Eqs. (77)-(79), no *a priori* assumption is made that the perturbations have small amplitudes compared to equilibrium quantities. The linear stability properties for small-amplitude perturbations about the primary signal are summarized in Sec. IV C, and the nonlinear saturation of a single sideband is estimated analytically in Sec. IV D.

The nonlinear evolution of the sideband instability is investigated in Sec. V. Following a general description of the numerical approach (Sec. V A), the evolution equation (77)-(79) are solved numerically for three sets of illustrative parameters [Cases I, II and III in Secs. V B and V C]. Two situations with different initial conditions are considered in Secs. V B and V C. In Sec. V B, the nonlinear evolution is determined numerically for small-amplitude initial conditions with wavenumber equal to that of the fastest growing mode. It is found in the numerical calculations for the three cases that the fastest growing mode, after an initial transient stage, grows exponentially with growth rate predicted by the analytical estimate in Sec. IV C. Moreover, the saturation amplitude is found to agree with the lower bound estimated in Sec. IV D. Cascade processes are examined in Sec. V C for the situation where the initial perturbations consist of sideband modes with wavenumber $\Delta K'_{\text{in}} = \Delta K'_M/2$. Here, $\Delta K'_M$ is the normalized wavenumber of the fastest growing mode. During the evolution, the nonlinear terms in Eqs. (101)-(103) generate harmonics of the initial perturbations. Included in these harmonics is the fastest growing sideband mode. For Cases I and III, which correspond to the strong-pump regime and the weak-pump regime, respectively, it is found in the early stage of evolution that the initial perturbations with wavenumber $\Delta K' = \Delta K'_M/2$ grow exponentially. However, before the sideband mode with $\Delta K' = \Delta K'_M/2$ can experience a significant growth, the fastest growing mode, which is excited by harmonic generation, has achieved a large amplitude. The fastest growing mode eventually causes the saturation of the sideband instability and dominates the long-term evolution of the system. On the other hand, for Case II, which corresponds to intermediate pump strength with $(\Omega'_B/\Gamma'_0)^2/4 = 1$, the initial perturbations with wavenumber $\Delta K' = \Delta K'_M/2$ grow without interference from the fastest growing mode, until they saturate at an amplitude comparable to the equilibrium amplitude \hat{a}_s^0 of the primary signal wave. Moreover, the fastest growing mode with $\Delta K' = \Delta K'_M$, which started with very small amplitude, evolves through harmonic

generation due to the strong influence of the large-amplitude sideband mode with $\Delta K' = \Delta K'_M/2$. It is also found that the long-term evolution for Case II involves many modes with comparable amplitudes interacting with one another.

In Sec. V D, the nonlinear evolution of the sideband instability is examined numerically for system parameters corresponding to the Los Alamos free electron laser.⁵ The dimensionless pump strength in this case is $(\Omega'_B/\Gamma'_0)^6/4 = 21$, and the maximum growth rate occurs at normalized wavenumber $\Delta K'_M = 1.195 \times 10^{-2} \simeq 1/84$. The initial conditions in the numerical calculation correspond to small-amplitude perturbations consisting of the first six Fourier components, i.e., $\Delta K' = m/252$, $m = 1, \dots, 6$. Following the time evolution of both the upper sideband signals and the lower sideband signals for the first six Fourier components, it is found that the lower sideband signal with wavenumber $\Delta K' = 1/84$ corresponds to the wavenumber $\Delta K'_M$ of the fastest growing mode. This mode experiences a large growth and achieves a power level comparable to the initial power in the primary signal. The power level of the primary signal, however, decreases from its initial value when the sideband signals grow to an appreciable level. Furthermore, the relative power spectrum $P(\Delta\omega)$, which is proportional to the amplitude-squared of the Fourier transform of $a_s^-(z_0, t)$ defined in Eq. (112) at $z = z_0$ in the laboratory frame, is obtained numerically in Sec. V D. It is found that a large peak in the sideband spectrum develops at a frequency which is downshifted by 2.2% from the frequency ω_s of the primary signal. This agrees qualitatively with the spectrum observed in the Los Alamos free electron laser experiment.⁵ The numerical calculation also shows, in good agreement with what has been observed in other numerical simulations,^{5,44} that the presence of the sideband signals increases the efficiency of radiation generation for a untapered wiggler field.

II. Theoretical Model and Assumptions

A. Basic Equations and Assumptions

The model consists of a tenuous relativistic electron beam propagating in the z direction through a constant-amplitude helical magnetic field with vector potential

$$\mathbf{A}_w(\mathbf{x}) = -(mc^2/e)a_w(\cos k_0 z \hat{\mathbf{e}}_x + \sin k_0 z \hat{\mathbf{e}}_y). \quad (1)$$

Here, $-e$ is the electron charge, mc^2 is the electron rest energy, $\lambda_w = 2\pi/k_0 = \text{const}$ is the wiggler wavelength, the wiggler magnetic field is $\mathbf{B}_w = \nabla \times \mathbf{A}_w$, and $a_w = e\hat{B}_w/mc^2 k_0$ is the normalized wiggler amplitude. The present analysis neglects longitudinal perturbations (Compton-regime approximation with $\delta\phi \simeq 0$), and transverse spatial variation ($\partial/\partial x = 0 = \partial/\partial y$). In addition to the static wiggler field in Eq.(1), it is assumed that a primary electromagnetic wave signal with right-circular polarization has developed with vector potential

$$\begin{aligned} \mathbf{A}_s(\mathbf{x}, t) = & (mc^2/e)\hat{a}_s(z, t)\{\cos[k_s z - \omega_s t + \delta_s(z, t)]\hat{\mathbf{e}}_x \\ & - \sin[k_s z - \omega_s t + \delta_s(z, t)]\hat{\mathbf{e}}_y\}, \end{aligned} \quad (2)$$

where the normalized amplitude $\hat{a}_s(z, t)$ and wave phase $\delta_s(z, t)$ are treated as slowly varying (eikonal approximation), and the corresponding electromagnetic fields are given by $\mathbf{B}_s = \nabla \times \mathbf{A}_s$, and $\mathbf{E}_s = -(1/c)\partial\mathbf{A}_s/\partial t$. The present analysis is carried out in the ponderomotive frame moving with axial velocity

$$v_p = \omega_s/(k_s + k_0), \quad (3)$$

relative to the laboratory frame. In the ponderomotive frame it is found that the transformed energy $\gamma'_j(t')$ is approximately constant, with $d\gamma'_j/dt' \simeq 0$ in the eikonal approximation. This simplifies considerably the treatment of the electron orbits in the combined wiggler field and the finite-amplitude primary electromagnetic wave.^{21-23,73,74,84}

The ponderomotive-frame variables (z', t', γ') are related to the laboratory-frame variables (z, t, γ) by the Lorentz transformation

$$\begin{aligned} z' &= \gamma_p(z - v_p t), \\ t' &= \gamma_p(t - v_p z/c^2), \\ \gamma' &= \gamma_p(\gamma - v_p p_z/mc^2), \end{aligned} \quad (4)$$

where $\gamma_p = (1 - v_p^2/c^2)^{-1/2}$ is the relativistic mass factor associated with the transformation, $\gamma' mc^2 = (m^2 c^4 + c^2 p_x'^2 + c^2 p_y'^2 + c^2 p_z'^2)^{1/2}$ is the mechanical energy, and the components of momentum (p_x', p_y', p_z') are related to the velocity $\mathbf{v}' = dx'/dt'$ by $\mathbf{p}' = \gamma' m \mathbf{v}'$.

In the ponderomotive frame, the slow nonlinear evolution of $\hat{a}_s(z', t')$ and $\delta'_s(z', t')$ is described by²⁴

$$2\omega'_s \left(\frac{\partial}{\partial t'} + \frac{k'_s c^2}{\omega'_s} \frac{\partial}{\partial z'} \right) \hat{a}_s = \frac{4\pi e^2 a_w}{m} \frac{1}{L'} \left\langle \sum_j \frac{\sin(\theta'_j + \delta'_s)}{\gamma'_j} \right\rangle, \quad (5)$$

$$2\omega'_s \hat{a}_s \left(\frac{\partial}{\partial t'} + \frac{k'_s c^2}{\omega'_s} \frac{\partial}{\partial z'} \right) \delta'_s = \frac{4\pi e^2 a_w}{m} \frac{1}{L'} \left\langle \sum_j \frac{\cos(\theta'_j + \delta'_s)}{\gamma'_j} \right\rangle, \quad (6)$$

where the real oscillation frequency ω'_s and wavenumber k'_s are related by the dispersion relation²⁴

$$\omega_s'^2 = c^2 k_s'^2 + \frac{4\pi e^2}{m} \frac{1}{L'} \left\langle \sum_j \frac{1}{\gamma'_j} \right\rangle. \quad (7)$$

In Eqs.(5)-(7), $\langle \sum_j \dots \rangle$ denotes a statistical average, and the axial orbit $\theta'_{j_s}(t') = k'_p z'_j(t')$ and energy $\gamma'_j(t')$ of the j th electron solve²⁴

$$\begin{aligned} \frac{d^2}{dt'^2} \theta'_{j_s} + \frac{c^2 k_p'^2 a_w}{\gamma_j'^2} \text{Im}[\hat{a}_s \exp(i\theta'_{j_s} + i\delta'_s)] \\ = \frac{c^2 k_p' a_w}{\gamma_j'^2} \text{Re} \left\{ \exp(i\theta'_{j_s}) \left(\frac{\partial}{\partial z'_j} + \frac{1}{c^2} \frac{dz'_j}{dt'} \frac{\partial}{\partial t'} \right) [\hat{a}_s \exp(i\delta'_s)] \right\}, \end{aligned} \quad (8)$$

and

$$\frac{d}{dt'} \gamma'_j = -\frac{a_w}{\gamma_j'} \text{Re} \left\{ \frac{\partial}{\partial t'} [\hat{a}_s \exp(i\delta'_s)] \right\}. \quad (9)$$

In Eqs.(8) and (9), the wavenumber k'_p of the ponderomotive potential is defined by

$$k'_p = (k_s + k_0)/\gamma_p, \quad (10)$$

and the relativistic mass factor γ'_j is defined by

$$\gamma_j'^2 = 1 + (p_{zj}'^2/m^2 c^2) + a_w^2 + \hat{a}_s^2 - 2a_w \text{Re}[\hat{a}_s \exp(i\theta'_{j_s} + i\delta'_s)] \quad (11)$$

in the ponderomotive frame. In obtaining Eqs.(8) and (9) from $dp'_{zj}/dt' = -mc^2 \partial \gamma'_j / \partial z'_j$ and $d\gamma'_j/dt' = \partial \gamma'_j / \partial t'$, we have neglected $\hat{a}_s^2 \ll 1 + a_w^2$ in Eq.(11). Moreover, it is assumed that all electrons have zero transverse canonical momentum, i.e., $P'_{xj} = 0 = P'_{yj}$.

There is some latitude in specifying the precise operational meaning³⁹ of the statistical averages $\langle \sum_j \dots \rangle$ occurring in Eqs.(5)-(7). For present purposes, let us assume that the orbits $z'_j(t')$ and $\gamma'_j(t')$ have been calculated from Eqs.(8) and (9) in terms of the initial values $z'_j(0)$ and $\gamma'_j(0)$. Then the simplest definition of the statistical average $\langle \sum_j \dots \rangle$ over some phase function $\Psi(\theta'_{j_s}(0), \gamma'_j(0))$ is given by

$$\frac{1}{L'} \left\langle \sum_j \Psi(\theta'_{j_s}(0), \gamma'_j(0)) \right\rangle = \hat{n}'_b \int_0^{2\pi} \frac{d\theta'_0}{2\pi} \int_1^\infty d\gamma'_0 G(\theta'_0, \gamma'_0) \Psi(\theta'_0, \gamma'_0). \quad (12)$$

Here, \hat{n}'_b is the average density of the beam electrons in the ponderomotive frame, and $G(\theta'_0, \gamma'_0)$ is the (probability) distribution of electrons in initial phase θ'_0 and energy γ'_0 . Moreover, $L' = 2\pi/k'_p$ is the basic periodicity length in the ponderomotive frame.

Equations (5)-(9) constitute a closed description of the nonlinear evolution of the system. In this regard further simplification of Eqs.(8) and (9) is possible by virtue of the assumption of slowly varying wave amplitude and phase (eikonal approximation), i.e.,

$$\begin{aligned} |\omega'_s| &\gg \left| [\hat{a}_s \exp(i\delta'_s)]^{-1} \frac{\partial}{\partial t'} [\hat{a}_s \exp(i\delta'_s)] \right|, \\ |k'_s| &\gg \left| [\hat{a}_s \exp(i\delta'_s)]^{-1} \frac{\partial}{\partial z'} [\hat{a}_s \exp(i\delta'_s)] \right|. \end{aligned} \quad (13)$$

In particular, to lowest order, it is valid to neglect the local temporal and spatial derivatives on the right-hand sides of Eqs.(8) and (9). This gives the approximate dynamical equations²⁴

$$\frac{d^2}{dt'^2} \theta'_{j_s} + \frac{c^2 k_p'^2 a_w}{\gamma_j'^2} \text{Im}[\hat{a}_s \exp(i\theta'_{j_s} + i\delta'_s)] = 0, \quad (14)$$

$$\frac{d}{dt'} \gamma'_j = 0. \quad (15)$$

The major benefit of carrying out the analysis in the ponderomotive frame is evident from Eqs.(14) and (15). To lowest order, the particle energy γ'_j can be treated as constant in Eqs.(5)-(9) and (14).

In circumstances where perturbations are about a primary electromagnetic wave with amplitude $\hat{a}_s^0 = \text{const}$ (independent of z' and t'), it is useful in analyzing the orbit equation (14) to introduce the bounce frequency $\hat{\omega}_B(\gamma'_j)$ defined by²¹

$$\hat{\omega}_B(\gamma'_j) = (c^2 k_p'^2 a_w \hat{a}_s^0 / \gamma_j'^2)^{1/2}. \quad (16)$$

Here, $a_w > 0$ and $\hat{a}_s^0 > 0$ are assumed without loss of generality, and $\hat{\omega}_B(\gamma'_j)$ is the effective bounce frequency of deeply trapped electrons with energy γ'_j . A detailed analysis²¹ of Eqs. (11) and (14) shows that the zero-order electron motion is *untrapped* for energies γ'_j satisfying (Fig.1)

$$\gamma'_j > \hat{\gamma}'_+ \equiv [1 + (a_w + \hat{a}_s^0)^2]^{1/2}. \quad (17)$$

That is, when Eq. (17) is satisfied, the particle motion is modulated by the ponderomotive potential, but the normalized velocity $d\theta'_{js}/dt'$ does not change polarity (Fig.1). On the other hand, for $\gamma'_j < \hat{\gamma}'_+$, the electrons are *trapped*, and the zero-order motion described by Eq. (14) is cyclic, corresponding to periodic motion in the ponderomotive potential. From Eqs. (11) and (14), it is readily shown that the minimum allowable energy of a trapped electron is²¹

$$\hat{\gamma}'_- \equiv [1 + (a_w - \hat{a}_s^0)^2]^{1/2}. \quad (18)$$

Because $\hat{a}_s^0 \ll a_w$ in the regimes of practical interest, we note from Eqs. (17) and (18) that the characteristic energy of a trapped electron is approximately

$$\hat{\gamma}' \equiv (1 + a_w^2)^{1/2}. \quad (19)$$

B. Conservation Relation

The evolution equation (5) for the wave amplitude $\hat{a}_s(z', t')$ and the orbit equation (14), together with the definition $\theta'_{js}(t') = k'_p z'_j(t')$, readily give

$$\left(\frac{\partial}{\partial t'} + \frac{k'_s c^2}{\omega'_s} \frac{\partial}{\partial z'} \right) \hat{a}_s^2 = - \frac{4\pi e^2}{m\omega'_s c^2 k'_p} \frac{1}{L'} \left\langle \gamma'_j \frac{d^2}{dt'^2} z'_{js} \right\rangle. \quad (20)$$

It will be shown in this section that Eq. (20) implies the conservation of energy in the laboratory frame.

Making use of the Lorentz transformation (4), the left-hand side of Eq.(20) can be expressed as

$$\left(\frac{\partial}{\partial t'} + \frac{k'_s c^2}{\omega'_s} \frac{\partial}{\partial z'} \right) \hat{a}_s^2 = \gamma_p \left(1 + \frac{v_p v'_g}{c^2} \right) \left(\frac{\partial}{\partial t} + v_g \frac{\partial}{\partial z} \right) \hat{a}_s^2, \quad (21)$$

where $v'_g = k'_s c^2 / \omega'_s$ is the group velocity of the electromagnetic wave in the ponderomotive frame, and

$$v_g = \frac{v'_g + v_p}{1 + v'_g v_p / c^2} \quad (22)$$

is the group velocity in the laboratory frame. The energy of the j th electron $\gamma_j m c^2$ in the laboratory frame is related to the ponderomotive frame variables γ'_j and p'_{zj} by

$$\gamma_j = \gamma_p \left(\gamma'_j + \frac{v_p p'_{zj}}{m c^2} \right) = \gamma_p \gamma'_j \left(1 + \frac{v_p}{c^2} \frac{dz'_j}{dt'} \right). \quad (23)$$

Operating on Eq.(23) with d/dt' gives

$$\frac{d}{dt'} \gamma_j = \frac{\gamma_p v_p \gamma'_j}{c^2} \frac{d^2}{dt'^2} z'_j. \quad (24)$$

In obtaining Eq.(24), use has been made of $d\gamma'_j/dt' = 0$ [Eq.(15)]. The characteristic velocity of an electron interacting with the ponderomotive potential can be estimated from the equation of motion (14). This gives $|d\theta'_j/dt'| \sim \hat{\omega}'_B(\gamma'_j)$, where the bounce frequency $\hat{\omega}'_B(\gamma'_j)$ is defined in Eq. (16). Therefore, $|dz'_j/dt'| \sim c(a_w \hat{a}_s^0)^{1/2} / \gamma'_j \ll c$ in the regime of practical interest, where a_w is of order unity and $\hat{a}_s^0 \ll 1$. That is to say the ponderomotive frame can be viewed (in an approximate sense) as the rest frame of the j th electron. Due to time dilation, the time derivative in the laboratory frame is related to the time derivative in the rest frame of the electron by $d/dt' = \gamma_p d/dt$. Therefore, Eq.(24) can be expressed in the equivalent form

$$\gamma'_j \frac{d^2}{dt'^2} z'_j = \frac{c^2}{v_p} \frac{d}{dt} \gamma_j. \quad (25)$$

The wave frequency and wavenumber (ω', k') in the ponderomotive frame are related to the wave frequency and wavenumber (ω, k) in the laboratory frame by

$$\begin{aligned} \omega' &= \gamma_p (\omega - k v_p), \\ k' &= \gamma_p (k - \omega v_p / c^2), \end{aligned} \quad (26)$$

where v_p is defined in Eq.(3) and $\gamma_p = (1 - v_p^2/c^2)^{-1/2}$. As a special case, for $(\omega, k) = (\omega_s, k_s)$ we obtain $\omega'_s = \gamma_p (\omega_s - k_s v_p)$ from Eq.(26), which gives

$$\omega'_s = \gamma_p k_0 v_p. \quad (27)$$

This is the familiar resonance condition for the free electron laser interaction.

Making use of (3), (10) (25) and (26), the right-hand side of Eq.(20) can be expressed as

$$-\frac{4\pi e^2}{m\omega'_s c^2 k'_p} \frac{1}{L'} \left\langle \gamma'_j \frac{d^2}{dt'^2} z'_{js} \right\rangle = -\frac{4\pi e^2}{m\gamma_p \omega_s (\omega_s - v_p k_s)} \frac{1}{L} \left\langle \frac{d}{dt} \gamma_j \right\rangle, \quad (28)$$

where the statistical average $\langle \sum_j \dots \rangle$ in the laboratory frame is related to that in the ponderomotive frame [Eq.(12)] by

$$\frac{1}{L} \langle \sum_j \dots \rangle = \gamma_p \frac{1}{L'} \langle \sum_j \dots \rangle. \quad (29)$$

In Eq.(29) $L^{-1} = \gamma_p L'^{-1}$, where the factor γ_p is due to the Lorentz contraction. Making use of Eqs. (26) and the definition $v'_g = k'_s c^2 / \omega'_s$, it can be shown that

$$1 + \frac{v_p v'_g}{c^2} = \frac{\omega_s}{\gamma_p^2 (\omega_s - v_p k_s)}. \quad (30)$$

It is evident from Eqs.(21) (28) and (30) that the conservation relation (20) is equivalent to the relation

$$\left(\frac{\partial}{\partial t} + v_g \frac{\partial}{\partial z} \right) \hat{a}_s^2 = -\frac{4\pi e^2}{m\omega_s^2} \frac{1}{L} \left\langle \frac{d}{dt} \gamma_j \right\rangle \quad (31)$$

in the laboratory frame.

To show that Eq. (31) implies energy conservation in the laboratory frame, we first define the average kinematic energy density of the beam electrons by

$$U_{\text{part}} = mc^2 \frac{1}{L} \left\langle \sum_j \gamma_j \right\rangle. \quad (32)$$

The energy of an electromagnetic wave in a dispersive dielectric medium is given by⁸⁷

$$\begin{aligned} U_{\text{em}} &= \frac{B_s^2}{8\pi} + \frac{\partial}{\partial \omega_s} [\omega_s K_{\text{em}}(k_s, \omega_s)] \frac{E_s^2}{8\pi} \\ &= \left[c^2 k_s^2 + \omega_s^2 K_{\text{em}}(k_s, \omega_s) + \omega_s^3 \frac{\partial K_{\text{em}}(k_s, \omega_s)}{\partial \omega_s} \right] \left(\frac{mc}{e} \right)^2 \frac{\hat{a}_s^2}{8\pi}, \end{aligned} \quad (33)$$

for a wave with slowly varying amplitude \hat{a}_s and phase δ'_s . Here, $K_{\text{em}}(k_s, \omega_s)$ is the transverse dielectric function for the medium. From Eqs. (7) and (26), it can be shown in the laboratory frame that the dispersion relation is

$$\omega_s^2 = c^2 k_s^2 + \omega_p^2. \quad (34)$$

Here, $K_{em}(k_s, \omega_s)$ is defined by (see Appendix A)

$$K_{em}(k_s, \omega_s) = \frac{c^2 k_s^2}{\omega_s^2} = 1 - \frac{\omega_p^2}{\omega_s^2}, \quad (35)$$

where the relativistic plasma frequency-squared ω_p^2 is defined by

$$\omega_p^2 = \frac{4\pi e^2}{m} \frac{1}{L'} \left\langle \sum_j \frac{1}{\gamma_j'} \right\rangle. \quad (36)$$

Substituting Eqs. (34) and (35) into Eq. (33) readily gives

$$U_{em} = \left(\frac{\omega_s m c}{e} \right)^2 \frac{\hat{a}_s^2}{4\pi}. \quad (37)$$

Making use of Eqs. (32) and (37), the conservation relation (31) can be expressed as

$$\frac{\partial}{\partial t} U_{em} + \frac{\partial}{\partial z} S_{em} + \frac{d}{dt} U_{part} = 0, \quad (38)$$

where $S_{em} = v_g U_{em}$ is the power flow density of the electromagnetic wave.

To summarize, Eq. (20) is equivalent to the energy conservation relation (38) in the laboratory frame. Furthermore, in the ponderomotive frame, Eq.(20) constitutes a powerful constraint condition in both analytical and numerical analyses.

C. Macroclump Model

To make the analytical investigation of the sideband instability tractable, we consider a simple model in which all of the beam electrons are trapped in the ponderomotive potential. Furthermore, the trapped electrons are assumed to be tightly bunched into coherent macroclumps. Under the assumptions of the macroclump model, the statistical average [Eq.(12)] over some phase function $\Psi(\theta'_{j_s}(0), \gamma'_j(0))$ is replaced by

$$\frac{1}{L'} \left\langle \sum_j \Psi(\theta'_{j_s}(0), \gamma'_j(0)) \right\rangle \rightarrow \hat{n}'_b \Psi(\theta'_{s,l'}, \gamma'_{l'}). \quad (39)$$

Here, \hat{n}'_b is the average density of the beam electrons in the ponderomotive frame, and the subscript $l' = k'_p z'$ (on $\theta'_{s,l'}$ and $\gamma'_{l'}$) is a label indicating that these variables are evaluated at the macroclump located in the ponderomotive potential at z' . Making use of Eq.(39), the field evolution equations (5) and (6) reduce to

$$\left(\frac{\partial}{\partial \tau'} + \frac{\partial}{\partial l'} \right) \hat{a}_s(l', \tau') = \epsilon'_p \sin[\theta'_{s,l'}(\tau') + \delta'_s(l', \tau')], \quad (40)$$

$$\hat{a}_s(l', \tau') \left(\frac{\partial}{\partial \tau'} + \frac{\partial}{\partial l'} \right) \delta'_s(l', \tau') = \epsilon'_p \cos[\theta'_{s,l'}(\tau') + \delta'_s(l', \tau')], \quad (41)$$

where $l' = k'_p z'$ and $\tau' = ck'_p t'$ are dimensionless space and time variables, respectively, and the dimensionless constant ϵ'_p is related to the system parameters by

$$\epsilon'_p ck'_p = \frac{a_w \hat{\omega}_{pb}^2}{2\omega'_s \hat{\gamma}'}. \quad (42)$$

Here, $\hat{\omega}_{pb}^2 = 4\pi\hat{n}'_b e^2/m$ is the nonrelativistic plasma frequency-squared in the ponderomotive frame. In obtaining Eqs. (40) and (41), it has been assumed that the electron beam has sufficiently low density that we can neglect beam dielectric effects and approximate $\omega'_s = ck'_s$. Furthermore, the energy γ'_j of the j th electron has been approximated by the characteristic energy $\hat{\gamma}' = (1 + a_w^2)^{1/2}$ defined in Eq. (19). Consistent with the eikonal approximation, the wave amplitude \hat{a}_s and phase δ'_s in Eqs. (40) and (41) change slowly with l' and τ' provided $|\epsilon'_p/\hat{a}_s| \ll 1$.

With regard to the evolution of $\theta'_{s,l'}$, it follows readily from Eq. (14) that

$$\frac{d^2}{d\tau'^2} \theta'_{s,l'}(\tau') + \epsilon'_w \hat{a}_s(l', \tau') \sin[\theta'_{s,l'}(\tau') + \delta'_s(l', \tau')] = 0, \quad (43)$$

where the dimensionless parameter ϵ'_w is defined by

$$\epsilon'_w = \frac{a_w}{\hat{\gamma}'^2}. \quad (44)$$

Here, we have approximated the energy γ'_j of the j th electron by the characteristic energy $\hat{\gamma}' = (1 + a_w^2)^{1/2}$ defined in Eq.(19). Making use of Eqs. (40) and (43), the following conservation relation is readily verified, i.e.,

$$\left(\frac{\partial}{\partial \tau'} + \frac{\partial}{\partial l'} \right) \hat{a}_s^2(l', \tau') = -\frac{2\epsilon'_p}{\epsilon'_w} \frac{d^2}{d\tau'^2} \theta'_{s,l'}(\tau'). \quad (45)$$

The coupled particle orbit equation (43) and field evolution equations (40) and (41), together with the conservation relation (45) will be used in subsequent sections to investigate the nonlinear dynamics of the sideband instability within the framework of the macroclump model.

III. Nonlinear Evolution of Primary Signal When $\partial/\partial l' = 0$

In this section we consider the evolution of the primary signal in circumstances where $\partial/\partial l' = 0$. This is the simplest application of the macroclump model to the nonlinear evolution of the free electron laser.

A. Basic Equations and Conservation Relations

When the evolution of the system is independent of l' ($\partial/\partial l' = 0$), Eqs. (40), (41) and (43) become

$$\frac{d}{d\tau'} \hat{a}_s(\tau') = \epsilon'_p \sin[\theta'_s(\tau') + \delta'_s(\tau')], \quad (46)$$

$$\hat{a}_s(\tau') \frac{d}{d\tau'} \delta'_s(\tau') = \epsilon'_p \cos[\theta'_s(\tau') + \delta'_s(\tau')], \quad (47)$$

$$\frac{d^2}{d\tau'^2} \theta'_s(\tau') = -\epsilon'_w \hat{a}_s(\tau') \sin[\theta'_s(\tau') + \delta'_s(\tau')], \quad (48)$$

which describe the nonlinear evolution of $\hat{a}_s(\tau')$, $\delta'_s(\tau')$ and $\theta'_s(\tau')$. The conservation relation (45) reduces to

$$\frac{d}{d\tau'} \left(\hat{a}_s^2 + \frac{2\epsilon'_p}{\epsilon'_w} \frac{d}{d\tau'} \theta'_s \right) = 0 \quad (49)$$

or

$$\frac{d}{d\tau'} \theta'_s + \frac{1}{2} \frac{\epsilon'_w}{\epsilon'_p} \hat{a}_s^2 = \dot{\theta}'_{s0} + \frac{1}{2} \frac{\epsilon'_w}{\epsilon'_p} \hat{a}_{s0}^2 = \text{const}, \quad (50)$$

where \hat{a}_{s0} and $\dot{\theta}'_{s0}$ denote initial values. In addition, it readily follows from Eqs. (46) and (47) that

$$\left(\frac{d}{d\tau'} \hat{a}_s \right)^2 + \left(\hat{a}_s \frac{d}{d\tau'} \delta'_s \right)^2 = \epsilon_p'^2 = \text{const}, \quad (51)$$

which is another useful conservation relation, valid when $\partial/\partial l' = 0$. Calculating $d^2 \hat{a}_s / d\tau'^2$ from Eqs. (46) and (47), we obtain

$$\begin{aligned} \frac{d^2}{d\tau'^2} \hat{a}_s &= \epsilon'_p \cos(\theta'_s + \delta'_s) \left(\frac{d\theta'_s}{d\tau'} + \frac{d\delta'_s}{d\tau'} \right) \\ &= \hat{a}_s \frac{d\delta'_s}{d\tau'} \left(\frac{d\theta'_s}{d\tau'} + \frac{d\delta'_s}{d\tau'} \right). \end{aligned} \quad (52)$$

Making use of Eqs. (50) and (51) to eliminate $d\theta'_s/d\tau'$ and $d\delta'_s/d\tau'$, it is readily shown that Eq.(52) reduces to

$$\begin{aligned} \frac{d^2}{d\tau'^2} \hat{a}_s &= \pm [\epsilon_p'^2 - (d\hat{a}_s/d\tau')^2]^{1/2} \\ &\times \left\{ \theta'_{s0} + \frac{1}{2} \frac{\epsilon_w'}{\epsilon_p'} (\hat{a}_{s0}^2 - \hat{a}_s^2) \pm \frac{1}{\hat{a}_s} [\epsilon_p'^2 - (d\hat{a}_s/d\tau')^2]^{1/2} \right\}. \end{aligned} \quad (53)$$

If we assume $\hat{a}_s > 0$, then the plus (minus) signs in Eq. (53) correspond to $d\delta'_s/d\tau' > 0$ ($d\delta'_s/d\tau' < 0$). Equation (53) is a closed nonlinear differential equation for the evolution of $\hat{a}_s(\tau')$ which can be solved subject to specified initial conditions $\hat{a}_s(\tau' = 0) = \hat{a}_{s0}$ and $d\hat{a}_s/d\tau'|_{\tau'=0} = \epsilon_p' \sin(\theta'_{s0} + \delta'_{s0})$.

B. Reduction to Quadrature

Equation (53), or equivalently, Eqs. (46)-(48) can be reduced to quadrature. Combining Eqs. (47) and (50) to form the combination $\hat{a}_s(d\delta'_s/d\tau' + d\theta'_s/\tau')$, it readily follows that

$$\hat{a}_s \frac{d}{d\tau'} (\theta'_s + \delta'_s) = \Delta\omega'_s \hat{a}_s - \frac{1}{2} \frac{\epsilon_w'}{\epsilon_p'} \hat{a}_s^3 + \epsilon_p' \cos(\theta'_s + \delta'_s), \quad (54)$$

where

$$\Delta\omega'_s \equiv \dot{\theta}'_{s0} + \frac{1}{2} \frac{\epsilon_w'}{\epsilon_p'} \hat{a}_{s0}^2. \quad (55)$$

For convenience, we introduce the rescaled variables A_s , Ψ'_s and ϵ'_s defined by

$$\begin{aligned} A_s &\equiv \sqrt{\frac{\epsilon_w'}{\epsilon_p'} \hat{a}_s}, \\ \Psi'_s &\equiv \theta'_s + \delta'_s, \\ \epsilon'_s &\equiv \sqrt{\epsilon_w' \epsilon_p'} = \left(\frac{a_w^2 \hat{\omega}_{pb}'^2}{2\omega'_s c k_p' \hat{\gamma}'^3} \right)^{1/2}. \end{aligned} \quad (56)$$

Then, Eqs. (46) and (54) can be expressed as

$$\frac{d}{d\tau'} A_s = \epsilon'_s \sin \Psi'_s, \quad (57)$$

$$A_s \left(\frac{d}{d\tau'} \Psi'_s - \Delta\omega'_s + \frac{1}{2} A_s^2 \right) = \epsilon'_s \cos \Psi'_s. \quad (58)$$

Nonlinear coupled amplitude-phase equations of the form (57) and (58) arise in several physical problems⁸¹⁻⁸³ and have a number of interesting properties. For example, it can be shown that $dC/d\tau' = 0$, where the constant of the motion C is defined

by

$$\begin{aligned}
C &= \epsilon'_s A_s \cos \Psi'_s + \frac{1}{2} \Delta \omega'_s A_s^2 - \frac{1}{8} A_s^4 \\
&= \epsilon'_s A_{s0} \cos \Psi'_{s0} + \frac{1}{2} \Delta \omega'_s A_{s0}^2 - \frac{1}{8} A_{s0}^4 \\
&= \text{const.}
\end{aligned} \tag{59}$$

Here, A_{s0} and Ψ'_{s0} denote initial values. Combining Eqs. (57) and (59), we readily obtain a closed first-order equation for the evolution of $A_s^2(\tau')$, i.e.,

$$\frac{1}{2} \left(\frac{d}{d\tau'} A_s^2 \right)^2 + V(A_s^2) = 0, \tag{60}$$

where the effective potential $V(A_s^2)$ is defined by

$$\begin{aligned}
V(A_s^2) &= 2 \left(\epsilon'_s A_{s0} \cos \Psi'_{s0} + \frac{1}{2} \Delta \omega'_s A_{s0}^2 - \frac{1}{8} A_{s0}^4 \right. \\
&\quad \left. - \frac{1}{2} \Delta \omega'_s A_s^2 + \frac{1}{8} A_s^4 \right)^2 - 2\epsilon_s'^2 A_s^2.
\end{aligned} \tag{61}$$

That is, use of the constant of the motion C defined in Eq.(59) has reduced the evolution of A_s^2 to quadrature in Eq. (60).

Equation (60) can be solved for a variety of initial conditions A_{s0} , Ψ'_{s0} and $\dot{\theta}'_{s0}$. For purposes of illustration, we assume

$$A_{s0} = 0, \quad \dot{\theta}'_{s0} = 0. \tag{62}$$

so that $\Delta \omega'_s = \dot{\theta}'_{s0} + \frac{1}{2} \frac{\epsilon'_w}{\epsilon'_p} \hat{a}_{s0}^2 = 0$, and

$$V(A_s^2) = \frac{1}{32} A_s^8 - 2\epsilon_s'^2 A_s^2. \tag{63}$$

It is evident from Eq. (60) that the maximum amplitude excursion $A_{s,\text{max}}$ satisfies $V(A_{s,\text{max}}^2) = 0$. Making use of Eqs. (60), (62) and (63), we obtain

$$A_{s,\text{max}} = 2(\epsilon_s')^{1/3}, \tag{64}$$

or equivalently [see Eqs. (42), (44) and (56)]

$$\hat{a}_{s,\text{max}} = 2 \frac{(\epsilon'_p)^{2/3}}{(\epsilon'_w)^{1/3}} = \left(\frac{2a_w \hat{\omega}_{pb}^4}{\omega_s'^2 c^2 k_p'^2} \right)^{1/3}. \tag{65}$$

Note that $\hat{a}_{s,\max}$ scales as $(\hat{n}'_b)^{2/3} a_w^{1/3}$, and except for a constant scale factor of order unity, the estimate of $\hat{a}_{s,\max}$ in (65) is the same as the estimate of the nonlinear saturation amplitude obtained in the high-gain Compton regime⁷⁵ using a simple trapping argument. To further illustrate this point, we introduce the dimensionless parameter $\Gamma'_0 \ll 1$ and the normalized (with respect to ck'_p) bounce frequency Ω'_B of a deeply trapped macroclump defined by

$$\Gamma_0'^3 = \frac{\epsilon'_w \epsilon'_p}{2} = \frac{a_w^2 \hat{\omega}_{pb}^2}{4\omega'_s \hat{\gamma}'^3 ck'_p}, \quad (66)$$

$$\Omega_B'^2 = \epsilon'_w \hat{a}_s^0 = \frac{a_w \hat{a}_s^0}{\hat{\gamma}'^2}. \quad (67)$$

In Eq. (66), $(3^{1/2}/2)\Gamma'_0 ck'_p$ is the familiar small-signal gain (temporal growth rate)⁷⁵ calculated in the ponderomotive frame. In the nonlinear regime, the saturation of the signal occurs when the characteristic bounce time $1/\Omega'_B$ of a trapped particle is comparable to the exponential-growth time $1/\Gamma'_0$. Therefore, the condition $\Gamma'_0 \simeq \Omega'_B$ gives an estimate of the amplitude at saturation. The saturation amplitude $\hat{a}_{s,\max}$ so estimated is the same as that obtained in Eq. (65), except for a constant scale factor of order unity.

IV. Sideband Instability for Primary Signal with Slowly Varying Phase

The basic framework for studying the sideband instability is established in this section. In Sec. IV A, we introduce an equilibrium model in which it is assumed that a primary wave signal with finite amplitude $\hat{a}_s^0 = \text{const}$ and slowly varying phase $\delta_s^0(l')$ is present in quasi-steady state. In Sec. IV B, use is made of Eqs. (40), (41) and (43) to derive the equations describing the nonlinear evolution of the sideband signal. In this regard, the sidebands are treated as perturbations about the quasi-steady state described in Sec. IV A. In deriving the equations for the nonlinear evolution of the sidebands, no *a priori* assumption is made that the perturbations have small amplitudes compared to equilibrium quantities. Linear stability properties of the primary signal are reviewed briefly in Sec. IV C, and the nonlinear saturation of a single sideband is estimated analytically in Sec. IV D. The dependence of the sideband saturation on the system parameters is found to scale differently in regimes characterized by the dimensionless pump parameter $(\Omega'_B/\Gamma'_0)^6/4$ [Eqs. (66) and (67)].

A. Equilibrium Model

For deeply trapped electrons, an appropriate quasi-steady equilibrium state consistent with Eqs. (40), (41) and (43) is described by

$$\begin{aligned}\theta_{s,l'}^0 + \delta_s^0 &= 2n\pi, \\ \frac{\partial}{\partial \tau'} \hat{a}_s^0 &= 0 = \frac{\partial}{\partial l'} \hat{a}_s^0,\end{aligned}\tag{68}$$

and

$$\frac{\partial}{\partial \tau'} \delta_s^0 = 0, \quad \hat{a}_s^0 \frac{\partial}{\partial l'} \delta_s^0 = \epsilon'_p,\tag{69}$$

where n is an integer. That is, the equilibrium wave amplitude \hat{a}_s^0 is constant (independent of l' and τ'), whereas there is a slow variation of wave phase δ_s^0 with l' described by Eq. (69). Making use of the dimensionless parameters Γ'_0 and Ω'_B defined in (66) and (67), respectively, Eq. (69) can then be expressed as

$$\frac{\partial}{\partial l'} \delta_s^0 = 2 \frac{\Gamma'_0{}^3}{\Omega'_B{}^2} = \frac{\epsilon'_p}{\hat{a}_s^0}.\tag{70}$$

Note that $2\Gamma_0^3/\Omega_B^2 = \epsilon'_p/\hat{a}_s^0 \ll 1$ is required in the present analysis in order that the change in δ_s^0 is small over the scale length of the ponderomotive potential ($\lambda'_p = 2\pi/k'_p$). Therefore, when we examine the stability properties in the weak-pump regime [$(\Omega'_B/\Gamma_0)^6/4 \ll 1$], it should be kept in mind that the limiting case where \hat{a}_s^0 approaches zero at finite value of the electron density is excluded in the subsequent analysis.

B. Evolution Equations for the Sideband Signals

In order to investigate the nonlinear evolution of the sideband signals, it is convenient to introduce the complex wave amplitude a_s , defined by

$$a_s(l', \tau') \equiv \hat{a}_s(l', \tau') \exp[i\delta'_s(l', \tau')]. \quad (71)$$

It follows directly from Eqs. (40) and (41) that

$$\left(\frac{\partial}{\partial \tau'} + \frac{\partial}{\partial l'} \right) a_s(l', \tau') = i\epsilon'_p \exp[-i\theta'_{s,\mu}(\tau')]. \quad (72)$$

Moreover, the orbit equation (43) for the macroclumps can be expressed in the equivalent form

$$\frac{d^2}{d\tau'^2} \theta'_{s,\mu}(\tau') + \epsilon'_w \text{Im}\{a_s \exp[i\theta'_{s,\mu}(\tau')]\} = 0. \quad (73)$$

We now express each dynamical variable as its equilibrium value plus a perturbation, i.e.,

$$\begin{aligned} \theta'_{s,\mu} &= \theta_{s,\mu}^0 + \delta\theta'_{s,\mu}, \\ a_s &= \hat{a}_s \exp(i\delta'_s) \equiv (\hat{a}_s^0 + \delta A_s) \exp(i\delta_s^0). \end{aligned} \quad (74)$$

Here, the equilibrium quantities \hat{a}_s^0 , δ_s^0 and $\theta_{s,\mu}^0$ are described by Eqs. (68) and (69) in Sec. IV A. Also note that the perturbed complex amplitude δA_s , of the electromagnetic wave is related to the perturbed real amplitude $\delta\hat{a}_s \equiv \hat{a}_s - \hat{a}_s^0$ and the perturbed phase $\hat{\delta}'_s \equiv \delta'_s - \delta_s^0$ by

$$\delta A_s = (\hat{a}_s^0 + \delta\hat{a}_s) \exp(i\hat{\delta}'_s) - \hat{a}_s^0. \quad (75)$$

When the perturbations are small, Eq. (75) reduces to

$$\delta A_s = \delta\hat{a}_s + i\hat{a}_s^0 \hat{\delta}'_s. \quad (76)$$

The equations of evolution for the perturbed quantities δA_s and $\delta\theta'_{s,\nu}$ can be obtained by substituting the definitions in Eq. (74) into Eqs. (72) and (73), and making use of Eqs. (68) and (69) to eliminate equilibrium quantities. This gives

$$\hat{a}_s^0 \left(\frac{\partial}{\partial \tau'} + \frac{\partial}{\partial l'} \right) \text{Re}(\delta A_s) = \epsilon'_p \left[\hat{a}_s^0 \sin(\delta\theta'_{s,\nu}) + \text{Im}(\delta A_s) \right], \quad (77)$$

$$\hat{a}_s^0 \left(\frac{\partial}{\partial \tau'} + \frac{\partial}{\partial l'} \right) \text{Im}(\delta A_s) = \epsilon'_p \left\{ \hat{a}_s^0 [\cos(\delta\theta'_{s,\nu}) - 1] - \text{Re}(\delta A_s) \right\}, \quad (78)$$

$$\begin{aligned} \frac{d^2}{d\tau'^2} \delta\theta'_{s,\nu} &= -\epsilon'_w \left\{ [\hat{a}_s^0 + \text{Re}(\delta A_s)] \sin(\delta\theta'_{s,\nu}) \right. \\ &\quad \left. + \text{Im}(\delta A_s) \cos(\delta\theta'_{s,\nu}) \right\}. \end{aligned} \quad (79)$$

In obtaining Eqs. (77)-(79), no *a priori* assumption has been made that the perturbations δA_s and $\delta\theta'_{s,\nu}$ are small. Therefore, Eqs. (77)-(79) can be used to study the *nonlinear* evolution of the sidebands within the framework of the macroclump model.

C. Linearized Equations for the Sideband Instability

The linear stability properties of the equilibrium state described in Sec. IV A have been studied by Davidson and Wurtele²⁴ in considerable detail. Here, we briefly review some of the key results which are relevant to the present analysis.

When the perturbations δA_s and $\delta\theta'_{s,\nu}$ are small, Eqs. (77)-(79) can be approximated by the linearized equations

$$\hat{a}_s^0 \left(\frac{\partial}{\partial \tau'} + \frac{\partial}{\partial l'} \right) \text{Re}(\delta A_s) = \hat{a}_s^0 \epsilon'_p (\delta\theta'_{s,\nu}) + \epsilon'_p \text{Im}(\delta A_s), \quad (80)$$

$$\hat{a}_s^0 \left(\frac{\partial}{\partial \tau'} + \frac{\partial}{\partial l'} \right) \text{Im}(\delta A_s) = -\epsilon'_p \text{Re}(\delta A_s), \quad (81)$$

$$\frac{d^2}{d\tau'^2} \delta\theta'_{s,\nu} = -\epsilon'_w [\hat{a}_s^0 \delta\theta'_{s,\nu} + \text{Im}(\delta A_s)]. \quad (82)$$

Examining normal-mode solutions to Eqs. (80)-(82), we assume that the τ' and l' dependence of the perturbations is proportional to $\exp[i(\Delta K'l' - \Delta\Omega'\tau')]$, where $\text{Im}(\Delta\Omega') > 0$ corresponds to instability (temporal growth). However, the perturbations $\text{Re}(\delta A_s)$, $\text{Im}(\delta A_s)$ and $\delta\theta'_{s,\nu}$ in Eqs. (80)-(82) are all real-valued. Therefore, the solutions to Eqs. (80)-(82) should be the sum of the complex normal-mode solu-

tions and their complex conjugates, i.e.,

$$\text{Re}(\delta A_s) = \alpha_s^r \exp[i(\Delta K'l' - \Delta\Omega'\tau')] + c. c., \quad (83)$$

$$\text{Im}(\delta A_s) = \alpha_s^i \exp[i(\Delta K'l' - \Delta\Omega'\tau')] + c. c., \quad (84)$$

$$\delta\theta_{s,\mu}^c = \delta\theta_s^c \exp[i(\Delta K'l' - \Delta\Omega'\tau')] + c. c., \quad (85)$$

where *c. c.* stands for complex conjugate, and α_s^r , α_s^i and $\delta\theta_s^c$ are complex amplitudes.

Substituting Eqs. (83)-(85) into Eqs. (80)-(82) gives the equations relating the amplitudes α_s^r , α_s^i and $\delta\theta_s^c$

$$-i\hat{a}_s^0(\Delta\Omega' - \Delta K')\alpha_s^r = \epsilon'_p(\hat{a}_s^0\delta\theta_s^c + \alpha_s^i), \quad (86)$$

$$-i\hat{a}_s^0(\Delta\Omega' - \Delta K')\alpha_s^i = -\epsilon'_p\alpha_s^r, \quad (87)$$

$$-(\Delta\Omega')^2\delta\theta_s^c = -\epsilon'_w(\hat{a}_s^0\delta\theta_s^c + \alpha_s^i). \quad (88)$$

For the perturbation amplitudes α_s^r , α_s^i and $\delta\theta_s^c$ in Eqs. (86)-(88) not to vanish, the frequency $\Delta\Omega'$ and wavenumber $\Delta K'$ must satisfy the dispersion relation

$$1 = \frac{\Omega_B'^2}{(\Delta\Omega')^2} + \frac{4\Omega_B'^2(\Gamma_0'/\Omega_B')^6}{(\Delta\Omega' - \Delta K')^2}, \quad (89)$$

which is the familiar dispersion relation obtained by Davidson and Wurtele²⁴ for the sideband instability assuming slowly varying equilibrium phase δ_s^0 and deeply trapped electrons. Here, the parameters Ω_B' and Γ_0' are defined in Eqs. (66) and (67).

Equation (89) has the familiar form of the dispersion relation for the two-stream instability.^{85,86} In the following special cases, the maximum growth rate $\text{Im}(\Delta\Omega')_M$ and the corresponding real frequency shift $\text{Re}(\Delta\Omega')_M$ and wavenumber $\Delta K'_M$ at maximum growth can be estimated analytically.²⁴

1. *Strong-pump regime* $[(\Omega_B'/\Gamma_0')^6/4 \gg 1]$

$$\begin{aligned} \text{Im}(\Delta\Omega')_M &= (3^{1/2}/2^{2/3})\Gamma_0'(\Gamma_0'/\Omega_B'), \\ \text{Re}(\Delta\Omega')_M &= \Omega_B' + (1/2^{2/3})\Gamma_0'(\Gamma_0'/\Omega_B'), \\ \Delta K'_M &= \Omega_B'. \end{aligned} \quad (90)$$

2. *Weak-pump regime* $[(\Omega'_B/\Gamma'_0)^6/4 \ll 1]$

$$\begin{aligned}\text{Im}(\Delta\Omega')_M &= (3^{1/2}/2)\Gamma'_0, \\ \text{Re}(\Delta\Omega')_M &= (1/2)\Gamma'_0, \\ \Delta K'_M &= 2\Gamma'_0(\Gamma'_0/\Omega'_B)^2.\end{aligned}\tag{91}$$

3. *Intermediate pump strength* $[(\Omega'_B/\Gamma'_0)^6/4 = 1]$

$$\begin{aligned}\text{Im}(\Delta\Omega')_M &= (1/2)\Omega'_B, \\ \text{Re}(\Delta\Omega')_M &= (3^{1/2}/2)\Omega'_B, \\ \Delta K'_M &= 3^{1/2}\Omega'_B.\end{aligned}\tag{92}$$

For three different values of the dimensionless pump parameter $(\Omega'_B/\Gamma'_0)^6/4$, Fig. 2 shows the plots versus normalized wavenumber $\Delta K'/\Omega'_B$ of the normalized growth rate $\text{Im}(\Delta\Omega')/\Omega'_B$. The maximum growth rate and the corresponding wavenumber for each pump parameter agree with those predicted in Eqs. (90)-(92).

D. Saturation Amplitude of the Fastest Growing Sideband

The unstable sideband modes obtained in Sec. IV C will grow exponentially until the assumptions used to derive the linearized equations (80)-(82) are violated. When linear theory breaks down, the nonlinear equations (77)-(79) should be used to determine the long-term evolution of the sideband modes. In Sec. V, Eqs. (77)-(79) will be solved numerically to determine the nonlinear evolution of the sideband instability within the framework of the macroclump model. In this section, we estimate analytically a lower bound on the saturation amplitude of the unstable sideband mode in the case where only the fastest growing mode is present. Although the fastest growing mode may generate harmonics, it is found from the growth rate curves in Fig. 2 that these harmonic modes are linearly stable with $\text{Re}\Delta\Omega' = 0$. Therefore, the harmonics do not experience significant growth before the breakdown of the linear theory.

The conditions for the breakdown of the linearized macroclump equations (80)-(82), as well as an estimate of the lower bound on the saturation amplitude are obtained from the following arguments.

(a) The nonlinear terms in the evolution equations (77)-(79) are: $\sin(\delta\theta'_{s,\nu})$ in Eq. (77); $\cos(\delta\theta'_{s,\nu}) - 1$ in Eq. (78); and $\sin(\delta\theta'_{s,\nu})$, $\text{Re}(\delta A_s) \sin(\delta\theta'_{s,\nu})$ and $\text{Im}(\delta A_s) \cos(\delta\theta'_{s,\nu})$ in Eq. (79). When $\sin(\delta\theta'_{s,\nu})$ and $\cos(\delta\theta'_{s,\nu})$ are expanded as power series in $\delta\theta'_{s,\nu}$, the terms $\cos(\delta\theta'_{s,\nu}) - 1$ and $\text{Re}(\delta A_s) \sin(\delta\theta'_{s,\nu})$ contain only products of even powers of perturbed quantities, and contribute only to the generation of even harmonics. Under the assumption that the linear growth rate of the fast growing mode is not affected by its own harmonics, as mentioned in the previous paragraph, we ignore the $\cos(\delta\theta'_{s,\nu}) - 1$ and $\text{Re}(\delta A_s) \sin(\delta\theta'_{s,\nu})$ terms in the saturation estimate. However, the other two terms, $\sin(\delta\theta'_{s,\nu})$ and $\text{Im}(\delta A_s) \cos(\delta\theta'_{s,\nu})$, contain triple products of the perturbed quantities, and the expansion procedure [e.g., $\sin(\delta\theta'_{s,\nu}) \simeq \delta\theta'_{s,\nu}$ and $\text{Im}(\delta A_s) \cos(\delta\theta'_{s,\nu}) \simeq \text{Im}(\delta A_s)$] breaks down when $\delta\theta'_{s,\nu}$ is of order unity.

(b) When $|\delta\theta'_{s,\nu}|$ is of order unity, nonlinear effects become important in the equation of motion (14) for a particle trapped in the ponderomotive potential. One such effect is that the bounce frequency of a trapped particle depends upon the amplitude of its bounce motion.

(c) In the regime where the linearized equations (80)-(82) are valid, the perturbations grow exponentially with relative amplitude obtained from Eqs. (83)-(88)

$$|\text{Im}(\delta A_s)| = \frac{1}{\epsilon'_w} \left| (\Delta\Omega')^2 - \epsilon'_w \hat{a}_s^0 \right| \cdot |\delta\theta'_{s,\nu}|, \quad (93)$$

$$|\text{Re}(\delta A_s)| = \frac{\hat{a}_s^0}{\epsilon'_w \epsilon'_p} \left| (\Delta\Omega' - \Delta K') [(\Delta\Omega')^2 - \epsilon'_w \hat{a}_s^0] \right| \cdot |\delta\theta'_{s,\nu}|. \quad (94)$$

When $|\delta\theta'_{s,\nu}|$ is of order unity, the linear theory breaks down. Hence the corresponding amplitude of the sideband can be estimated by setting $|\delta\theta'_{s,\nu}| \simeq 1$ in Eqs. (93) and (94). This gives

$$|\text{Im}(\delta A_s)/\hat{a}_s^0| \simeq \frac{1}{\epsilon'_w \hat{a}_s^0} \left| (\Delta\Omega')^2 - \epsilon'_w \hat{a}_s^0 \right|, \quad (95)$$

$$|\text{Re}(\delta A_s)/\hat{a}_s^0| \simeq \frac{1}{\epsilon'_w \epsilon'_p} \left| (\Delta\Omega' - \Delta K') [(\Delta\Omega')^2 - \epsilon'_w \hat{a}_s^0] \right|, \quad (96)$$

as the conditions for the linear theory to break down. Since the amplitude of the unstable sideband grows exponentially until the linear theory breaks down, the amplitudes in Eqs. (95) and (96) determine a lower bound on the saturation amplitude. The *lowest* estimate in Eqs. (95) and (96) is the one of physical interest. Furthermore,

it will become evident in Sec. V, that the amplitudes $\text{Re}(\delta A_s)$ and $\text{Im}(\delta A_s)$ are closely related to the amplitudes of the upper and lower sideband signals [Eqs. (107), (108), (114) and (115)].

To examine the scaling of the saturation amplitude, we now substitute the complex frequency and real wavenumber estimated analytically in Eqs. (90)-(92) for the fastest growing mode into Eqs. (95) and (96). This gives the following estimates:

1. *Strong-pump regime* $[(\Omega'_B/\Gamma'_0)^6/4 \gg 1]$

$$\begin{aligned} |\text{Im}(\delta A_s)/\hat{a}_s^0|_{\text{sat}} &\gtrsim 2^{2/3} \left[\frac{\epsilon_p'^2}{\epsilon_w'(\hat{a}_s^0)^3} \right]^{1/3} = 2^{4/3} \left(\frac{\Gamma'_0}{\Omega'_B} \right)^2, \\ |\text{Re}(\delta A_s)/\hat{a}_s^0|_{\text{sat}} &\gtrsim 2^{1/3} \left[\frac{\epsilon_p'^2}{\epsilon_w'(\hat{a}_s^0)^3} \right]^{1/6} = 2^{2/3} \left(\frac{\Gamma'_0}{\Omega'_B} \right). \end{aligned} \quad (97)$$

2. *Weak-pump regime* $[(\Omega'_B/\Gamma'_0)^6/4 \ll 1]$

$$\begin{aligned} |\text{Im}(\delta A_s)/\hat{a}_s^0|_{\text{sat}} &\gtrsim \frac{1}{2^{2/3}\hat{a}_s^0} \left(\frac{\epsilon_p'}{\epsilon_w'} \right)^{1/3} = \left(\frac{\Gamma'_0}{\Omega'_B} \right)^2, \\ |\text{Re}(\delta A_s)/\hat{a}_s^0|_{\text{sat}} &\gtrsim \frac{1}{2^{2/3}\hat{a}_s^0} \left(\frac{\epsilon_p'}{\epsilon_w'} \right)^{1/3} = \left(\frac{\Gamma'_0}{\Omega'_B} \right)^2. \end{aligned} \quad (98)$$

3. *Intermediate pump strength* $[(\Omega'_B/\Gamma'_0)^6/4 = 1]$

$$\begin{aligned} |\text{Im}(\delta A_s)/\hat{a}_s^0|_{\text{sat}} &\gtrsim 1, \\ |\text{Re}(\delta A_s)/\hat{a}_s^0|_{\text{sat}} &\gtrsim 1. \end{aligned} \quad (99)$$

It is evident from Eq. (97) in the strong-pump regime $[(\Omega'_B/\Gamma'_0)^6/4 \gg 1]$, that the sideband signal may saturate at an amplitude smaller than that of the primary signal \hat{a}_s^0 . However, when the pump strength $(\Omega'_B/\Gamma'_0)^6/4$ is of order unity in Eq. (99), the sideband signal may grow to an amplitude at least comparable to \hat{a}_s^0 .

In the weak-pump regime, Eq. (98) gives a saturation amplitude larger than \hat{a}_s^0 . It is interesting to note, apart from a factor of order unity, that the saturation amplitude in (98) is equal to $\hat{a}_{s,\text{max}}$ in Eq. (65) obtained for the nonlinear evolution of the primary signal when $\partial/\partial l' = 0$. As mentioned in Sec. III, the amplitude $\hat{a}_{s,\text{max}}$ is the same as the nonlinear saturation amplitude of primary signal in the high-gain Compton regime using simple trapping arguments.⁷⁵ It should also be pointed out that the maximum growth rate (normalized with respect to ck'_p) in the weak-pump regime,

$(\sqrt{3}/2)\Gamma'_0$ from Eq. (91), is the familiar small-signal gain (temporal growth rate)⁷⁵ calculated in the ponderomotive frame.

Assuming that an unstable sideband is present, it is important to note that the excursion of a macroclump about its equilibrium unperturbed position will grow to a significant amplitude, i.e., $|\delta\theta'_{s,\nu}| \sim 1$, no matter how small the initial amplitude of the unstable sideband. This should be compared with the result obtained by Riyopoulos and Tang,²⁷ who have shown, when only a single sideband with constant amplitude (independent of z and t) is present, that the motion of the particles becomes highly irregular only if the amplitude of the sideband is greater than some threshold value.

It should be reiterated that the estimate of the saturation amplitude carried out in this section is valid only for single-mode sideband excitation. When many sideband modes are present simultaneously, coupling between sideband modes becomes important, which renders the present estimate of the saturation amplitude invalid. Also the present estimates of the saturation amplitude are restricted to the fastest growing mode. For modes with smaller growth rates, cascade processes (Sec. V) may generate harmonics which grow faster than the fundamental mode.

As a final point, the lower bounds on the saturation amplitude in Eqs. (97)-(99) have been estimated earlier in this section by taking the maximum excursion of the macroclump in Eqs. (93) and (94) to be $|\delta\theta'_{s,\nu}| \simeq 1$. The numerical results in Sec. V B, however, suggest that the maximum excursion $|\delta\theta'_{s,\nu}|_{\max}$ is comparable to π [see Figs. 3(c), 4(c) and 5(c)]. Moreover, the field amplitudes $|\text{Re}(\delta a_s)|$ and $|\text{Im}(\delta a_s)|$ are observed to saturate at amplitudes larger than the lower bounds in Eqs. (97)-(99) by a factor between unity and π (see Figs. 3-5).

V. Nonlinear Evolution of the Sideband Instability

A. General Description

Equations (77)-(79) are solved numerically in this section in order to examine the nonlinear evolution of the sideband instability. First, a few key points are described regarding the procedure used to analyse the coupled nonlinear differential equations (77)-(79).

By making the change of variable

$$\xi' = l' - \tau', \quad (100)$$

the partial differential equations (77) and (78) reduce to the ordinary differential equations

$$\hat{a}_s^0 \frac{d}{d\tau'} \text{Re}[\delta A_s(\xi', \tau')] = \epsilon'_p \left\{ \hat{a}_s^0 \sin[\delta\theta'_{s,l'}(\tau')] + \text{Im}[\delta A_s(\xi', \tau')] \right\}, \quad (101)$$

$$\hat{a}_s^0 \frac{d}{d\tau'} \text{Im}[\delta A_s(\xi', \tau')] = \epsilon'_p \left\{ \hat{a}_s^0 \{ \cos[\delta\theta'_{s,l'}(\tau')] - 1 \} - \text{Re}[\delta A_s(\xi', \tau')] \right\}. \quad (102)$$

Moreover, the macroclump equation of motion (79) becomes

$$\begin{aligned} \frac{d^2}{d\tau'^2} \delta\theta'_{s,l'}(\tau') = & -\epsilon'_w \left(\{ \hat{a}_s^0 + \text{Re}[\delta A_s(\xi', \tau')] \} \sin[\delta\theta'_{s,l'}(\tau')] \right. \\ & \left. + \text{Im}[\delta A_s(\xi', \tau')] \cos[\delta\theta'_{s,l'}(\tau')] \right). \end{aligned} \quad (103)$$

In Eqs. (101)-(103), the subscript l' on $\delta\theta'_{s,l'}$ indicates that the corresponding macroclump is located at $l' = k'_p z'$. It is evident from Eqs. (68) and (69) that l' is a discrete label with incremental value $2\pi/(1 + \epsilon'_p/\hat{a}_s^0)$, where $\epsilon'_p/\hat{a}_s^0 \ll 1$ is assumed to be consistent with the assumption that the wave phase δ'_s varies slowly [see Eq. (70)]. Furthermore, the field perturbation δA_s is a function of τ' and ξ' . In the present analysis, the fast spatial variation on the length scale $L' = 2\pi/k'_p$ has been eliminated by averaging over an interval of length L' . Therefore, at given τ' , the change in δA_s is small when ξ' changes by an amount of order unity. Furthermore, it is an appropriate approximation to consider ξ' as a discrete label. For present purposes, we chose the incremental value of ξ' to be the same as that of the label l' , i.e., $\Delta\xi' = \Delta l' = 2\pi/(1 + \epsilon'_p/\hat{a}_s^0)$. To evaluate the right-hand side of Eqs. (101) and (102) for a particular value of ξ' , the corresponding value of l' in $\delta\theta'_{s,l'}$ is determined by

minimizing the difference $|\xi' - (l' - \tau')|$. Note that $|\xi' - (l' - \tau')|$ is generally nonzero, because ξ' and l' are both discrete labels. Similarly, to evaluate the right-hand side of Eq. (103) for a particular value of l' , the same condition is used to determine the value of ξ' in $\delta A_s(\xi', \tau')$.

For convenience in the numerical calculations, we also assume the periodic boundary conditions

$$\begin{aligned}\delta\theta'_{s,l'+L_p} &= \delta\theta'_{s,l'}, \\ \delta A_s(\xi' + L_p, \tau') &= \delta A_s(\xi', \tau'),\end{aligned}\quad (104)$$

where the spatial periodicity length L_p is defined by

$$L_p = 2\pi N_{\text{pot}} / (1 + \epsilon'_p / \hat{a}_s^0), \quad (105)$$

and N_{pot} is the number of ponderomotive potentials in each period. For the periodic boundary conditions in Eq. (104), the sideband modes allowed in the system are those with wavenumber $\Delta K' = 2\pi m / L_p$ ($m = 1, 2, 3, \dots$). That is, the resolution in wavenumber ($\Delta K'$ -space) is sacrificed by assuming the periodic boundary conditions in Eq. (104). Nevertheless, the present calculation is still a multimode analysis, so that nonlinear effects such as harmonic generation and the coupling between allowed discrete modes are taken into account.

It is useful to express the dynamics variables $\delta\theta'_{s,l'}(\tau')$ and $\delta A_s(\xi', \tau')$ in terms of the Fourier series

$$\delta\theta'_{s,l'}(\tau') = \delta\theta_0(\tau') + \sum_{\Delta K'} \delta\theta_{\Delta K'}(\tau') \cos[\Delta K'(l' - \tau') + \Psi_{\Delta K'}^\theta(\tau')], \quad (106)$$

$$\text{Re}[\delta A_s(\xi', \tau')] = \delta A_0^r(\tau') + \sum_{\Delta K'} \delta A_{\Delta K'}^r(\tau') \cos[\Delta K'\xi' + \Psi_{\Delta K'}^r(\tau')], \quad (107)$$

$$\text{Im}[\delta A_s(\xi', \tau')] = \delta A_0^i(\tau') + \sum_{\Delta K'} \delta A_{\Delta K'}^i(\tau') \cos[\Delta K'\xi' + \Psi_{\Delta K'}^i(\tau')], \quad (108)$$

where the wavenumber $\Delta K'$ is restricted by the periodic boundary conditions in Eq. (104) to be $\Delta K' = 2\pi m / L_p$ ($m = 1, 2, 3, \dots$). The Fourier coefficients in Eqs. (106)-(108) are related to the real-valued variables $\delta\theta'_{s,l'}(\tau')$ and $\delta A_s(\xi', \tau')$ by

$$\delta\theta_{\Delta K'}(\tau') \exp[i\Psi_{\Delta K'}^\theta(\tau')] = \frac{2}{N_{\text{pot}}} \sum_{l'=mL_p/N_{\text{pot}}}^{m=1, \dots, N_{\text{pot}}} \delta\theta'_{s,l'}(\tau') \exp[-i\Delta K'(l' - \tau')],$$

$$\begin{aligned}
\delta A_{\Delta K'}^r(\tau') \exp[i\Psi_{\Delta K'}^r(\tau')] &= \frac{2}{N_{\text{pot}}} \sum_{\xi'=mL_p/N_{\text{pot}}}^{m=1,\dots,N_{\text{pot}}} \text{Re}[\delta A_s(\xi', \tau')] \exp(-i\Delta K'\xi'), \\
\delta A_{\Delta K'}^i(\tau') \exp[i\Psi_{\Delta K'}^i(\tau')] &= \frac{2}{N_{\text{pot}}} \sum_{\xi'=mL_p/N_{\text{pot}}}^{m=1,\dots,N_{\text{pot}}} \text{Im}[\delta A_s(\xi', \tau')] \exp(-i\Delta K'\xi'),
\end{aligned} \tag{109}$$

and

$$\begin{aligned}
\delta\theta_0(\tau') &= \frac{1}{N_{\text{pot}}} \sum_{l'=mL_p/N_{\text{pot}}}^{m=1,\dots,N_{\text{pot}}} \delta\theta'_{s,l'}(\tau'), \\
\delta A_0^r(\tau') &= \frac{1}{N_{\text{pot}}} \sum_{\xi'=mL_p/N_{\text{pot}}}^{m=1,\dots,N_{\text{pot}}} \text{Re}[\delta A_s(\xi', \tau')], \\
\delta A_0^i(\tau') &= \frac{1}{N_{\text{pot}}} \sum_{\xi'=mL_p/N_{\text{pot}}}^{m=1,\dots,N_{\text{pot}}} \text{Im}[\delta A_s(\xi', \tau')].
\end{aligned} \tag{110}$$

Making use of Eqs. (69) and (71), and substituting $\xi' = l' - \tau'$ into Eqs. (107) and (108), the complex amplitude a_s defined in Eq. (71) can be expressed in the equivalent form

$$\begin{aligned}
a_s(l', \tau') &= [\delta A_0^r(\tau') + \hat{a}_s^0 + i\delta A_s^i(\tau')] \exp(i\epsilon'_p l' / \hat{a}_s^0) \\
&+ \frac{1}{2} \sum_{\Delta K'} \{ \delta A_{\Delta K'}^r(\tau') \exp[i\Psi_{\Delta K'}^r(\tau')] + i\delta A_{\Delta K'}^i(\tau') \exp[i\Psi_{\Delta K'}^i(\tau')] \} \\
&\quad \times \exp[i\Delta K'(l' - \tau')] \exp(i\epsilon'_p l' / \hat{a}_s^0) \\
&+ \frac{1}{2} \sum_{\Delta K'} \{ \delta A_{\Delta K'}^r(\tau') \exp[-i\Psi_{\Delta K'}^r(\tau')] + i\delta A_{\Delta K'}^i(\tau') \exp[-i\Psi_{\Delta K'}^i(\tau')] \} \\
&\quad \times \exp[-i\Delta K'(l' - \tau')] \exp(i\epsilon'_p l' / \hat{a}_s^0).
\end{aligned} \tag{111}$$

For the right-circularly polarized electromagnetic wave with vector potential defined in Eq. (2), we introduce the complex representation of the vector potential

$$a_s^-(z, t) = a_{zs}(z, t) - ia_{yx}(z, t). \tag{112}$$

Making use of Eq. (2) and the inverse of the Lorentz transformation (4), it is readily shown that

$$\begin{aligned}
a_s^-(z', t') &= \hat{a}_s(z', t') \exp[i(k'_s z' - \omega'_s t') + i\delta_s(z', t')] \\
&= a_s(z', t') \exp[i(k'_s z' - \omega'_s t')],
\end{aligned} \tag{113}$$

where (ω'_s, k'_s) in the ponderomotive frame is related to (ω_s, k_s) in the laboratory frame by Eq. (26). For convenience, we introduce the definitions

$$A_{\Delta K'}^u(\tau') \exp[i\psi_{\Delta K'}^u(\tau')] = \frac{1}{2} \{ \delta A_{\Delta K'}^r(\tau') \exp[i\Psi_{\Delta K'}^r(\tau')] + i\delta A_{\Delta K'}^i(\tau') \exp[i\Psi_{\Delta K'}^i(\tau')] \}, \quad (114)$$

$$A_{\Delta K'}^l(\tau') \exp[i\psi_{\Delta K'}^l(\tau')] = \frac{1}{2} \{ \delta A_{\Delta K'}^r(\tau') \exp[-i\Psi_{\Delta K'}^r(\tau')] + i\delta A_{\Delta K'}^i(\tau') \exp[-i\Psi_{\Delta K'}^i(\tau')] \}, \quad (115)$$

$$A_p(\tau') \exp[i\psi_p(\tau')] = [\delta A_0^r(\tau') + \hat{a}_s^0 + i\delta A_s^i(\tau')], \quad (116)$$

where $A_{\Delta K'}^u$, $A_{\Delta K'}^l$, $\psi_{\Delta K'}^u$ and $\psi_{\Delta K'}^l$ are real-valued functions. It is evident from Eqs. (111)-(115) and the definitions $l' = k'_p z'$ and $\tau' = ck'_p t'$, that $A_{\Delta K'}^u(\tau')$ is the amplitude of the upper sideband with wavenumber k' upshifted from the wavenumber k'_s of the primary wave by $\Delta k' = \Delta K' k'_p$, and that the corresponding real frequency ω' is upshifted from the frequency ω'_s of the primary wave by $\text{Re}(\Delta\omega') = ck'_p [\Delta K' - (d\psi_{\Delta K'}^u/d\tau')]$. Similarly, the amplitude of the lower sideband with wavenumber k' downshifted from the wavenumber k'_s of the primary wave by $\Delta k' = \Delta K' k'_p$ is $A_{\Delta K'}^l(\tau')$ defined in Eq. (115), and the corresponding real frequency ω' is downshifted from the frequency ω'_s of the primary wave by $\text{Re}(\Delta\omega') = ck'_p [\Delta K' + (d\psi_{\Delta K'}^l/d\tau')]$. Furthermore, the quantity $A_p(\tau')$ defined in Eq. (116) is the amplitude of the primary wave, and $ck'_p(-d\psi_p/d\tau')$ is the real frequency shift of the primary wave from the frequency ω'_s .

As a final remark on the numerical approach used to investigate the sideband instability, the conservation relation in Eq. (45) is a useful constraint condition, which can be used to test the accuracy of numerical calculations. Integrating Eq. (45) with respect to l' over a periodicity length L_p readily gives

$$\frac{d}{d\tau'} \int_0^{L_p} dl' \hat{a}_s^2(l', \tau') = -\frac{2\epsilon'_p}{\epsilon'_w} \frac{d}{d\tau'} \sum_{l'=mL_p/N_{\text{pot}}}^{m=1, \dots, N_{\text{pot}}} \frac{d}{d\tau'} \theta'_{s,l'}(\tau'), \quad (117)$$

or equivalently,

$$\int_0^{L_p} dl' \hat{a}_s^2(l', \tau') + \frac{2\epsilon'_p}{\epsilon'_w} \sum_{l'=mL_p/N_{\text{pot}}}^{m=1, \dots, N_{\text{pot}}} \frac{d}{d\tau'} \theta'_{s,l'}(\tau') = \text{const.} \quad (118)$$

during the nonlinear evolution of the sideband instability. In subsequent sections, the constraint condition in Eq. (118) is used as a check on numerical accuracy.

B. Exponential Growth and Saturation

The nonlinear evolution of the sideband instability has been investigated by solving Eqs. (101)-(103) numerically over a wide range of system parameters, subject to the periodic boundary conditions in Eq. (104). It is evident from Eqs. (101)-(103) that the nonlinear evolution of the free electron laser depends on the three dimensionless parameters ϵ'_p , ϵ'_w and \hat{a}_s^0 defined in Eqs. (42), (44) and (68). In this regard, it should be kept in mind that $\epsilon'_p \ll \hat{a}_s^0$ is required in order to be consistent with the assumption that the amplitude \hat{a}_s and phase δ'_s of the electromagnetic wave vary slowly in comparison with the fast temporal scale $1/ck'_p$ and the fast spatial scale $1/k'_p$. Moreover, the variables l' and ξ' are discretized as described in Sec. V A.

For purposes of illustration, we choose three sets of illustrative parameters, corresponding the strong-pump, intermediate-pump and weak-pump regimes.

Case I: $\epsilon'_p = 3.1623 \times 10^{-7}$, $\epsilon'_w = 0.1$ and $\hat{a}_s^0 = 10^{-3}$

In this case, the pump strength $[(\Omega'_B/\Gamma'_0)/4]^6 = \epsilon'_w(\hat{a}_s^0)^3/\epsilon'^2_p = 10^3$, which corresponds to the strong-pump regime. The growth rate, real frequency shift and the wavenumber of the fastest growing mode obtained from Eqs. (66), (67) and (90) are

$$\text{Im}(\Delta\Omega')_M = 6.87 \times 10^{-4}, \quad \text{Re}(\Delta\Omega')_M = 10^{-2}, \quad \Delta K'_M = 10^{-2}. \quad (119)$$

The lower bound on the saturation amplitude obtained from Eq. (97) gives

$$\left| \text{Im}(\delta A_s)/\hat{a}_s^0 \right|_{\text{sat}} \gtrsim 1.59 \times 10^{-1}, \quad \left| \text{Re}(\delta A_s)/\hat{a}_s^0 \right|_{\text{sat}} \gtrsim 3.98 \times 10^{-1}. \quad (120)$$

Case II: $\epsilon'_p = 5.807 \times 10^{-6}$, $\epsilon'_w = 3.37 \times 10^{-2}$ and $\hat{a}_s^0 = 10^{-3}$

In this section, the pump strength $[(\Omega'_B/\Gamma'_0)/4]^6 = \epsilon'_w(\hat{a}_s^0)^3/\epsilon'^2_p = 1.0$, which corresponds to the intermediate-pump regime. The growth rate, real frequency shift and the wavenumber of the fastest growing mode obtained from Eqs. (66), (67) and (92) are

$$\text{Im}(\Delta\Omega')_M = 2.9 \times 10^{-3}, \quad \text{Re}(\Delta\Omega')_M = 5.0 \times 10^{-3}, \quad \Delta K'_M = 10^{-2}. \quad (121)$$

The lower bound on the saturation amplitude obtained from Eq. (99) gives

$$\left| \text{Im}(\delta A_s)/\hat{a}_s^0 \right|_{\text{sat}} \gtrsim 1.0, \quad \left| \text{Re}(\delta A_s)/\hat{a}_s^0 \right|_{\text{sat}} \gtrsim 1.0. \quad (122)$$

Case III: $\epsilon'_p = 10^{-6}$, $\epsilon'_w = 10^{-3}$ and $\hat{a}_s^0 = 10^{-4}$.

In this case, the pump strength $[(\Omega'_B/\Gamma'_0)/4]^6 = \epsilon'_w(\hat{a}_s^0)^3/\epsilon_p'^2 = 10^{-3}$, which corresponds to the weak-pump regime. The growth rate, real frequency shift and the wavenumber of the fastest growing mode obtained from Eqs. (66), (67) and (91) are

$$\text{Im}(\Delta\Omega')_M = 6.87 \times 10^{-4}, \quad \text{Re}(\Delta\Omega')_M = 3.97 \times 10^{-4}, \quad \Delta K'_M = 10^{-2}. \quad (123)$$

The lower bound on the saturation amplitude obtained from Eq. (98) gives

$$\left| \text{Im}(\delta A_s) / \hat{a}_s^0 \right|_{\text{sat}} \gtrsim 6.3, \quad \left| \text{Re}(\delta A_s) / \hat{a}_s^0 \right|_{\text{sat}} \gtrsim 6.3. \quad (124)$$

The nonlinear evolution is determined numerically for small-amplitude initial conditions with wavenumber equal to that of the fastest growing mode. That is, the wavenumber of the initial perturbation is equal to $\Delta K'_M$ defined in Eqs. (119), (121) and (123) for Cases I, II and III, respectively. For the three cases considered here, the wavenumber $\Delta K'_M$ is equal to 10^{-2} . For specified $\Delta K'$, note that the dispersion relation (89) has four roots. Therefore, initial perturbations with wavenumber $\Delta K'$ are generally linear combinations of these modes. Figures 3-5 show the time evolution of the Fourier amplitudes with $\Delta K' = \Delta K'_M = 10^{-2}$. The Fourier decompositions defined in Eqs. (106)-(109) are used to obtain the Fourier amplitudes $\delta A_{\Delta K'}^r$, $\delta A_{\Delta K'}^i$ and $\delta\theta_{\Delta K'}$ from the variables $\delta A_s(\xi', \tau')$ and $\delta\theta'_{s,\mu}(\tau')$, which are obtained directly by solving Eqs. (101)-(103). It is evident from Figs. 3-5 that the perturbations, after an initial transient stage, grow exponentially with growth rates predicted by Eqs. (119), (121) and (123), until the linear theory breaks down. Moreover, the saturation amplitudes in Figs. 3-5 are found to agree with the lower bounds estimated in Eqs. (120), (122) and (124), within a factor of three. In addition, the following features are found in the numerical calculations.

(a) During exponential growth, the real frequency shift of the fastest growing sideband modes agrees with that given in Eqs. (119), (121) and (123).

(b) Before saturation, the higher harmonics of the initial perturbations have amplitudes much smaller than the amplitude of the fastest growing mode, as anticipated from the linear theory.

(c) After the fastest growing mode saturates, it is found in the numerical calculation for Case II with dimensionless pump strength $(\Omega'_B/\Gamma'_0)^6/4 = 1$ that the

harmonics with $\Delta K' = 2\Delta K'_M$ and $\Delta K' = 3\Delta K'_M$ can grow to an amplitude comparable to that of the fastest growing mode (approximately \hat{a}_s^0). In contrast, the fastest growing modes in Cases I and III remain the only dominant sidebands in the long-term evolution of the system.

In summary, the time evolution of the fastest growing sideband mode has been studied for three choices of system parameters. The three stages observed in the evolution correspond to an initial transient followed by exponential growth and saturation. The numerical examples presented in this section confirm the validity of the analytical estimates of the growth rate and saturation amplitude in Secs. IV C and IV D over a wide range of system parameters.

C. Cascade Processes

In this section, we examine a situation where the initial perturbations consist of sideband modes with wavenumber $\Delta K'_{\text{in}} = \Delta K'_M/2$. Here, $\Delta K'_M$ is the wavenumber of the fastest growing mode. During the evolution, harmonics of the initial perturbations are generated by the nonlinear terms in Eqs. (101)-(103). Included in these harmonics is the fastest growing sideband mode. In the situation examined in this section, the long-term evolution of the instability behaves differently for different choices of system parameters. To demonstrate this, we present three examples with system parameters ϵ'_p , ϵ'_w and \hat{a}_s^0 identical to Cases I, II and III in Sec. V B. It follows from Eqs. (119), (121) and (123) that the wavenumber $\Delta K'_{\text{in}}$ of the initial perturbations is equal to 0.5×10^{-2} , and that of the fastest growing mode is $\Delta K'_M = 10^{-2}$ in all three cases. Figures 6-8 show the evolution of the Fourier amplitudes $\delta A_{\Delta K'}^r$ and $\delta A_{\Delta K'}^i$ for the sideband signals with wavenumbers $\Delta K'_{\text{in}} = \Delta K'_M/2$ and $\Delta K'_M$, and system parameters corresponding to Cases I, II and III, respectively.

For Case I with system parameters $\epsilon'_p = 3.1623 \times 10^{-7}$, $\epsilon'_w = 0.1$ and $\hat{a}_s^0 = 10^{-3}$, which corresponds to the strong-pump regime, the results displayed in Figs. 6(a) and 6(b) show that the initial perturbations with wavenumber $\Delta K'_{\text{in}} = \Delta K'_M/2$ grow exponentially, after a short transient stage. The observed growth rate agrees with that obtained from the dispersion relation in Eq. (89). However, the exponential growth of the initial perturbations saturates at an amplitude much smaller than what would

be predicted, had we assumed single-mode evolution and applied Eqs. (95) and (96) to estimate the saturation amplitude in the present case. The failure of the single-mode assumption is evident from Figs. 6(c) and 6(d), which show that the fastest growing mode, after being excited by harmonic generation, grows with the growth rate given in Eq. (119) and eventually causes the breakdown of the linear theory. The evolution of the fastest growing mode in Figs. 6(c) and 6(d) is similar to that shown in Figs. 4(a) and 4(b), except for a time delay, which is a consequence of the different initial conditions used in the two calculations. The amplitudes of the higher harmonics, which are not shown here, are small compared to the amplitude of the fastest growing mode. Therefore, in this case, which corresponds to the strong-pump regime, the evolution of the system is dominated by the fastest growing mode with wavenumber $\Delta K' = \Delta K'_M$.

Figures 7(a)-7(d) show the evolution of the system for Case II with parameters $\epsilon'_p = 5.807 \times 10^{-6}$, $\epsilon'_w = 3.37 \times 10^{-2}$ and $\hat{a}_s^0 = 10^{-3}$. The dimensionless pump parameter $(\Omega'_B/\Gamma'_0)^6/4$ is equal to unity in this case. It is evident from Fig. 2(b) that the unstable sideband mode with $\Delta K' = \Delta K'_{in} = \Delta K'_M/2$ has growth rate comparable to that of the fastest growing mode with $\Delta K' = \Delta K'_M$. It is observed in Figs. 7(a) and 7(b) that the initial perturbations grow exponentially with a growth rate which agrees with that obtained from the dispersion relation in Eq. (89). Moreover, before saturation at an amplitude of the same order as the equilibrium amplitude \hat{a}_s^0 of the primary signal wave, the exponential growth continues without interference from the fastest growing mode. On the other hand, the fastest growing mode with $\Delta K' = \Delta K'_M$, which started with very small amplitude, evolves through harmonic generation due to the strong influence of the large-amplitude sideband mode with $\Delta K' = \Delta K'_M/2$. In the present situation, it is evident from Figs. 7(c) and 7(d) that the fastest growing mode behaves very differently from the single-dominant-mode case shown in Figs. 4(a) and 4(b). Although, within certain time intervals, the evolution in Figs 7(c) and 7(d) does behave like exponential growth, the growth rate does not agree with that obtained from the dispersion relation in Eq. (89). It is also found during the exponential growth of the sideband mode with $\Delta K' = \Delta K'_M/2$ that all of the higher harmonics (not shown in Fig. 7) have amplitudes small compared to the amplitude of the sideband mode with $\Delta K' = \Delta K'_M/2$. In the long-term evolution, however, many of the higher harmonics

eventually grow to amplitudes comparable to that of the sideband mode with $\Delta K' = \Delta K'_M/2$. Therefore, in this case, which corresponds to the intermediate-pump regime, the long-term evolution involves many modes with comparable amplitudes interacting with one another.

Displayed in Figs. 8(a)-8(d) is the evolution for Case III with system parameters $\epsilon'_p = 10^{-6}$, $\epsilon'_w = 10^{-3}$ and $\hat{a}_s^0 = 10^{-4}$, which corresponds to the weak-pump regime. Comparing Figs. 2(a) and 2(c), it is evident that the growth rate curve for this case has the same shape as that for Case I. Therefore, it is not surprising to find in Figs. 8(a)-8(d) that the fastest growing mode dominates the evolution. The amplitudes of the higher harmonics, which are not shown here, remain small compared to the amplitude of the fastest growing mode during the evolution. In the present calculation, the time evolution of the fastest growing mode shown in Figs. 8(c) and 8(d) is similar to the single-dominant-mode case shown in Figs. 5(a) and 5(b), except for a time delay due to the difference in initial conditions. The oscillatory behavior observed in Figs. 8(a) and 8(b) is attributed to the interference between different sideband modes in the initial perturbations. As discussed in Sec. V B, for each wavenumber $\Delta K'$, there are four modes corresponding to the four roots obtained from the dispersion relation in Eq. (89). The initial perturbations chosen for the case in Fig. 8 happen to contain large contributions from two oscillatory modes. The interference between these modes generates the oscillatory pattern in Figs. 8(a) and 8(b). A similar pattern is also observed in Figs. 5(a) and 5(b) during the transient stage. Depending on the initial conditions, this interference can also occur in the strong-pump and intermediate-pump regimes.

D. Nonlinear Evolution for System Parameters Corresponding to the Los Alamos Free Electron Laser

The first experimental investigation of the free electron laser sideband instability was carried out by Warren, *et al*⁵ at Los Alamos using an L-band RF linear accelerator operating at 20MeV, peak current of 40A, and micropulse width of ~ 35 ps. The electron beam has radius $r = 1$ mm, which gives an estimated density $\hat{n}_b = 2.65 \times 10^{11} \text{cm}^{-3}$ in the laboratory frame. The wiggler magnets generate a transverse planar

wiggler field with constant wavelength $\lambda_w = 2.73\text{cm}$ and constant amplitude $B_w = 3\text{kG}$ which corresponds to a normalized wiggler amplitude $a_w = 0.76$. The total length of the wiggler is $L=1\text{m}$.

The laser oscillator operates at an output wavelength of $\lambda_s = 10.35\mu\text{m}$.⁵ The peak laser output power inferred from the micropulse width is about 5MW from the coupler (or 100MW in the cavity).⁵ The radius of the optical beam at the center of the wiggler is 1.45mm, which gives the estimate $\hat{a}_s = 2.4 \times 10^{-4}$ for the normalized amplitude of the radiation field.

The velocity $v_p = \beta_p c$ of the ponderomotive potential defined in Eq. (3) is determined from $\beta_p = \lambda_w/(\lambda_w + \lambda_s) = 0.99962$ (or equivalently $1 - \beta_p = 3.8 \times 10^{-4}$), and the relativistic mass factor $\gamma_p = (1 - \beta_p^2)^{-1/2}$ associated with the Lorentz transformation is $\gamma_p = 36.2$. The value of the wavenumber k'_p of the ponderomotive potential defined in Eq. (10) is readily determined to be $k'_p = 1.68 \times 10^2\text{cm}^{-1}$. Making use of Eq. (27), the frequency ω'_s of the primary signal in the ponderomotive frame is $\omega'_s = 2.5 \times 10^{12}\text{rad/sec}$. The nonrelativistic plasma frequency-squared is defined by $\hat{\omega}_{pb}^2 = 4\pi\hat{n}_b e^2/m$, where $\hat{n}_b = \hat{n}_b/\gamma_p$ is the electron density in the ponderomotive frame. In this experiment, the electron density is $\hat{n}_b \simeq 2.65 \times 10^{11}\text{cm}^{-3}$, which gives $\hat{\omega}_{pb}^2 = 2.33 \times 10^{19}\text{sec}^{-2}$.

To determine the dimensionless parameters ϵ'_p and ϵ'_w corresponding to the Los Alamos free electron laser,⁵ we make use of the definitions in Eqs. (19), (42) and (44). Making use of the values of the system parameters calculated earlier in this section, this gives $\epsilon'_p = 5.6 \times 10^{-7}$ and $\epsilon'_w = 0.48$. Furthermore, we take the normalized amplitude of the radiation field to be the equilibrium amplitude of the primary signal, i.e., $\hat{a}_s^0 = 2.4 \times 10^{-4}$. Substituting the calculated values of the dimensionless parameters ϵ'_p , ϵ'_w and \hat{a}_s^0 into the definitions in Eqs. (66) and (67), readily gives the dimensionless pump strength $(\Omega'_B/\Gamma'_0)^6/4 = 21$ for the parameters corresponding to the Los Alamos free electron laser.

The dispersion relation in Eq. (89) has been solved for the set of system parameters corresponding to $\epsilon'_p = 5.6 \times 10^{-7}$, $\epsilon'_w = 0.48$ and $\hat{a}_s^0 = 2.4 \times 10^{-4}$. This gives the plots versus real wavenumber $\Delta K'$ of the growth rate $\text{Im}(\Delta\Omega'_s)$ and real frequency shift $\text{Re}(\Delta\Omega'_s)$ displayed in Fig.9. The maximum normalized growth rate is approximately

2.3×10^{-3} , which occurs at wavenumber $\Delta K'_M = 1.195 \times 10^{-2}$.

Equations (77)-(79) have been solved numerically to determine nonlinear evolution of the sideband instability for the choice of system parameters $\epsilon'_p = 5.6 \times 10^{-7}$, $\epsilon'_s = 0.48$ and $\hat{a}_s^0 = 2.4 \times 10^{-4}$, using 252 periods of the ponderomotive potential ($N_{\text{pot}} = 252$) and the boundary conditions in Eq. (104). The allowed wavenumbers are $\Delta K' = m/252$, where $m = 1, 2, \dots$. Moreover, $m = 3$ or $\Delta K' = 1/84$ is approximately equal to the wavenumber $\Delta K'_M = 1.195 \times 10^{-2}$ of the fastest growing mode. The initial conditions in the numerical calculation correspond to small-amplitude perturbations consisting of the first six Fourier components, i.e., $m = 1, \dots, 6$, which are assumed to have equal amplitudes at $\tau' = 0$.

Figures 10(a)-10(f) show the time evolution of the normalized power $P_{\Delta K'}$ of the upper sideband signal (dotted curve) and lower sideband signal (solid curve) for the first six Fourier components with wavenumbers $\Delta K' = m/252$, $m = 1, \dots, 6$. Here, the normalized power $P_{\Delta K'}$ is defined by

$$P_{\Delta K'} = \begin{cases} [A_{\Delta K'}^u(\tau')/\hat{a}_s^0]^2, & \text{upper sideband,} \\ [A_{\Delta K'}^l(\tau')/\hat{a}_s^0]^2, & \text{lower sideband,} \end{cases} \quad (125)$$

where $A_{\Delta K'}^u(\tau')$ and $A_{\Delta K'}^l(\tau')$ are defined in Eqs. (114) and (115). It is evident from Figs. 10(a)-10(f) that both the upper sideband and the lower sideband for all six Fourier components experience significant growth in amplitude. Most remarkable is the lower sideband for $\Delta K' = 1/84$, which corresponds to the fastest growing mode and achieves a power level comparable to the initial power in the primary signal. Another sideband signal which also distinguishes itself from the other sideband signals by growing to a large power level (more than one tenth of the power of the primary signal) is the lower sideband for $\Delta K' = 1/42$. Figures 11(a) and 11(b) show the real frequency shifts $(-d\psi'_{\Delta K'}/d\tau' - \Delta K')$ [see the paragraph following Eqs. (114)-(116)] of the lower sideband signals for both $\Delta K' = 1/84$ and $\Delta K' = 1/42$. It is found from Fig. 11(a) that the real frequency shift of the lower sideband signal for $\Delta K' = 1/84$ is approximately $\text{Re}(\Delta\Omega') = 0.01$ (in units normalized with respect to ck'_p). Making use of the inverse transform of Eq. (26), the real frequency shift in the laboratory frame (in real unit) is determined from $\text{Re}\Delta\omega_s = \gamma_p(\text{Re}\Delta\Omega' + \beta_p\Delta K')ck'_p = 4 \times 10^{12}\text{rad/sec}$, which is approximately 2.2 percent of the primary signal frequency $\omega_s = 2\pi c/\lambda_s = 1.82 \times 10^{14}\text{rad/sec}$. As a final remark on the results displayed in Figs. (10) and (11), it

is found in the present calculation that a large peak in the sideband spectrum develops at a frequency which is downshifted by 2.2% from that of the primary signal. This is in qualitative agreement with what is observed in the experiment.⁵

Figures 12(a) and 12(b) show the evolution of the normalized power $A_p^2/(\hat{a}_s^0)^2$ for the primary signal [see Eq. (116) and the paragraph following Eq. (116)] and the normalized spatially averaged power $\langle \hat{a}_s^2 \rangle / (\hat{a}_s^0)^2$, respectively. Here, the spatial average $\langle \hat{a}_s^2 \rangle$ of the field amplitude-squared is defined by

$$\begin{aligned} \langle \hat{a}_s^2(\tau') \rangle &= \frac{1}{L_p} \int_0^{L_p} \hat{a}_s^2(l', \tau') dl' \\ &= A_p^2(\tau') + \sum_{l'=mL_p/N_{\text{pot}} \substack{m=1, \dots, N_{\text{pot}}}} \{ [A_{\Delta K'}^u(\tau')]^2 + [A_{\Delta K'}^l(\tau')]^2 \}, \end{aligned} \quad (126)$$

which includes the contributions from the primary signal and the sideband signals. In obtaining Eq. (126), use has been made of Eqs. (71), (111) and (114)-(116).

It is evident from Fig. 12(a) that the power level of the primary signal decreases from its initial value when the sideband signals grow to an appreciable level. However, it is found from Fig. 12(b) that the total radiated power, which includes the contributions from the primary signal as well as the sideband signals, becomes larger than its initial value, during the long-term evolution. This implies, in good agreement with what has been observed in other numerical simulations,^{5,44} that the presence of the sideband signals increases the efficiency of radiation generation for a untapered wiggler field.

It is interesting to examine the power spectrum in the laboratory frame of the electromagnetic field obtained in the numerical calculation modeling the Los Alamos free electron laser. Making use of Eqs. (4) and (113), the complex amplitude $a_s^-(z, t)$ defined in Eq. (112) in the laboratory frame is readily obtained from $a_s(z', t')$ calculated numerically. At a point z_0 in the laboratory frame, the power spectrum is proportional to the amplitude-squared of the Fourier transform of $a_s^-(z_0, t)$. Figures 13(a) and 13(b) show the relative power $P(\Delta\omega)$ plotted versus the normalized frequency shift $\Delta\omega/\omega_s$ from the frequency ω_s of the primary signal. The vertical axes in Figs. 13(a) and 13(b) have been rescaled so that the maximum of $P(\Delta\omega)$ is equal to unity. The difference between Figs. 13(a) and 13(b) is the following. In taking the Fourier transform to obtain the plot in Fig. 13(a), the data for the entire evolution

from $\tau' = 0$ to $\tau' = 6000$ are used. On the other hand, in obtaining the plot in Fig. 13(b), only the data from $\tau' = 4000$ to $\tau' = 6000$ are used. It is evident from Figs. 13(a) and 13(b) that a strong sideband signal develops at a frequency which is downshifted by approximately 2.2% from the frequency ω_s of the primary signal. During the later stages of evolution (from $\tau' = 4000$ to $\tau' = 6000$), it is found in Fig. 13(b) that the lower sideband signal at $\Delta\omega/\omega_s = -2.2\%$ has a larger power output than the primary signal. Moreover, the primary signal experiences a small frequency shift to somewhat higher frequency.

In summary, there are several areas of qualitative agreement between the results of the Los Alamos free electron laser experiment⁵ and those of the present macro-clump model. Nevertheless, it should be kept in mind, when making the comparison, that there are significant differences between the present model and the experimental situation. Besides the simplifications associated with neglecting space charge effects and transverse spatial variations, the present model differs from the experiment in the following aspects.

(a) The present model assumes a helical wiggler field, whereas the experiment uses a planar wiggler field.

(b) The present model assumes that the interaction region is infinite in the z direction and satisfies the periodic boundary conditions in Eq. (104). In the experiment, however, the wiggler field, electron pulses and optical pulses have finite length.

(c) In the ponderomotive frame, the wiggler field of length L_w (measured in the laboratory frame) passes by a beam electron in a time interval $T_p = L_w/(\gamma_p v_p)$, which is approximately $T_p = 9.2 \times 10^{-11}$ sec for $L_w = 1$ m, $v_p \simeq c$ and $\gamma_p = 36.2$. The total evolution time $\tau' = 6000$ (or $t' = \tau'/ck'_p = 1.2 \times 10^{-9}$ sec) in the numerical calculation corresponds to 130 passes of electrons pulses (or 130 bounces in the cavity of the optical pulse). In the experiment, the electrons are distributed uniformly within the pulse at the beginning of each pass. The present model, however, assumes that the electrons are tightly bunched into macroclumps during the entire evolution of the system.

VI. Conclusions

In this paper, we have investigated the nonlinear evolution of the sideband instability within the framework of a simple macroclump model. The model is based on the field evolution equations (5) and (6), and the particle orbit equations (14) and (15). A conservation relation [Eq. (20)], associated with the self-consistent evolution of the electromagnetic field and the particles orbits, was obtained in the ponderomotive frame, and shown to be equivalent to energy conservation in the laboratory frame (Sec. II B). In the macroclump model, the beam electrons are assumed to be trapped and tightly bunched into coherent macroclumps. This leads to a simplification in the evolution equations (Sec. II C).

Within the framework of the macroclump model, assuming $\partial/\partial t' = 0$ in the ponderomotive frame, the nonlinear evolution of the primary signal was examined in Sec. III. It was found that the evolution equations (46)-(48) can be reduced to quadrature [Eq. (60)]. The maximum excursion $A_{s,\max}$ was determined analytically for the choice of initial conditions $A_{s0} = 0$ and $\theta'_{s0} = 0$ in Eq. (62). This gives a maximum amplitude of the primary signal $\hat{a}_{s,\max} = 2(\epsilon'_p)^{2/3}/(\epsilon'_w)^{1/3} = [2a_w \hat{\omega}_{pb}^4 / \omega_s'^2 c^2 k_p'^2]^{1/3}$ [Eq. (65)], which is the same (within a factor of order unity) as the estimate of the nonlinear saturation amplitude obtained in the high-gain Compton regime⁷⁵ using a simple trapping argument.

The coupled differential equations (77)-(79) were derived, which describe the nonlinear evolution of the sideband signals. In obtaining Eqs. (77)-(79), no *a priori* assumption was made that the sideband signals have small amplitudes compared to equilibrium quantities. Linear stability properties were summarized for small-amplitude perturbations about the equilibrium state described by Eqs. (68) and (69) (Sec. IV C), and the saturation amplitude of the fastest growing sideband was estimated analytically (Sec. IV D).

For three sets of illustrative parameters [see Cases I, II and III in Secs. V B and V C], a detailed investigation of the nonlinear evolution of the sideband instability was carried out by solving Eqs. (77)-(79) numerically. Moreover, the nonlinear evolution of the sideband instability was investigated numerically for system parameters corresponding to the Los Alamos free electron laser experiment (Sec. V D). In several

aspects, the numerical results were found to be in good qualitative agreement with the experimental results.

In conclusion, the nonlinear evolutions equations (77)-(79) were investigated analytically and numerically over a wide range of system parameters to determine detailed scaling properties of the sideband stability within the framework of the macroclump model. The present analysis suggests that a free electron laser operating with system parameters corresponding to the strong-pump regime [$(\Omega'_B/\Gamma'_0)^6/4 = \epsilon'_w (\hat{a}_s^0)^3/\epsilon'_p{}^2 \gg 1$] is less vulnerable to the sideband instability than a free electron laser operating in the weak-pump regime or in the intermediate-pump regime. Furthermore, it has been shown in a recent kinetic analysis of the sideband instability by Yang and Davidson⁸⁴ that a sufficiently large energy spread in the trapped-electron distribution can reduce significantly the growth rate of the unstable sidebands for system parameters corresponding to the strong-pump regime [$(\Omega'_B/\Gamma'_0)^6/4 \gg 1$]. Therefore, we conclude by suggesting that the strong-pump regime is the most favorable regime for free electron laser operation, as far as amelioration of the sideband instability is concerned.

Acknowledgements

This research was supported by the National Science Foundation, and in part by the Department of Energy High Energy Physics Division, the Naval Research Laboratory Plasma Physics Division, and the Office of Naval Research. The research by one of the authors (T.-Y. B. Yang) was in partial fulfillment of the requirements for the Ph.D. degree.

Appendix A. Derivation of the Dielectric Function in the Laboratory Frame

From Eq. (7), the transverse dielectric function $K'_{em}(k'_s, \omega'_s)$ in the ponderomotive frame for an electromagnetic wave propagating in the z direction is

$$K'_{em}(k'_s, \omega'_s) = \frac{c^2 k'^2_s}{\omega'^2_s} = 1 - \frac{\omega_p^2}{\omega'^2_s}, \quad (\text{A1})$$

where the relativistic plasma frequency-squared ω_p^2 is defined by

$$\omega_p^2 = \frac{4\pi e^2}{m} \frac{1}{L'} \left\langle \sum_j \frac{1}{\gamma_j} \right\rangle. \quad (\text{A2})$$

Equation (A1) is the familiar dielectric function for a transverse electromagnetic wave propagating in an unmagnetized plasma including relativistic effects. The electric field \mathbf{E}'_s of the electromagnetic wave is related to the perturbed current density \mathbf{J}'_s of the beam electrons by

$$4\pi \mathbf{J}'_s = -i\omega'_s [K'_{em}(k'_s, \omega'_s) - 1] \mathbf{E}'_s. \quad (\text{A3})$$

Here, both the current density \mathbf{J}'_s and the electric field \mathbf{E}'_s are perpendicular to the z direction. Therefore, the current density \mathbf{J}'_s and the electric field \mathbf{E}'_s in the ponderomotive frame are related to the laboratory-frame variables \mathbf{J}_s and \mathbf{E}_s by⁸⁸

$$\mathbf{J}'_s = \mathbf{J}_s, \quad (\text{A4})$$

$$\mathbf{E}'_s = \gamma_p \left(\mathbf{E}_s + \frac{v_p}{c} \hat{e}_z \times \mathbf{B}_s \right). \quad (\text{A5})$$

Making use of the Faraday's law

$$ik_s \hat{e}_z \times \mathbf{E}_s = \frac{i\omega_s}{c} \mathbf{B}_s, \quad (\text{A6})$$

Eq. (A5) can be expressed as

$$\mathbf{E}'_s = \gamma_p \left(1 - \frac{v_p k_s}{\omega_s} \right) \mathbf{E}_s, \quad (\text{A7})$$

where k_s and ω_s are the wavenumber and frequency, respectively, of the electromagnetic wave in the laboratory frame.

Substituting Eqs. (A4) and (A7) into Eq. (A3) readily gives

$$\begin{aligned} 4\pi \mathbf{J}_s &= -i\omega'_s [K'_{em}(k'_s, \omega'_s) - 1] \gamma_p \left(1 - \frac{v_p k_s}{\omega_s} \right) \mathbf{E}_s \\ &= -i\omega_s [K_{em}(k_s, \omega_s) - 1] \mathbf{E}_s, \end{aligned} \quad (\text{A8})$$

where the dielectric function $K_{em}(k_s, \omega_s)$ in the laboratory frame is defined by

$$K_{em}(k_s, \omega_s) = 1 + \frac{\omega'_s}{\omega_s} [K'_{em}(k'_s, \omega'_s) - 1] \gamma_p \left(1 - \frac{v_p k_s}{\omega_s} \right). \quad (\text{A9})$$

Making use of Eqs. (A1) and (A9) and the transformation (26) between (ω_s, k_s) and (ω'_s, k'_s) , we obtain

$$K_{em}(k_s, \omega_s) = 1 - \frac{\omega_p^2}{\omega_s^2} \quad (\text{A10})$$

in the laboratory frame.

References

- ¹C. A. Brau, IEEE J. Quantum Electron. **QE-21**, 824 (1985).
- ²T. J. Orzechowski, B. Anderson, W. M. Fawley, D. Prosnitz, E. T. Scharlemann, S. Yarema, D. B. Hopkins, A. C. Paul, A. M. Sessler and J. S. Wurtele, Phys. Rev. Lett. **54**, 889 (1985).
- ³T. J. Orzechowski, E. T. Scharlemann, B. Anderson, V. K. Neil, W. M. Fawley, D. Prosnitz, S. M. Yarema, D. B. Hopkins, A. C. Paul, A. M. Sessler and J. S. Wurtele, IEEE J. Quantum Electron. **QE-21**, 831 (1985).
- ⁴M. Billardon, P. Elleaume, J. M. Ortega, C. Bazin, M. Bergher, M. Velghe, D. A. G. Deacon and Y. Petroff, IEEE J. Quantum Electron. **QE-21**, 805 (1985).
- ⁵R. W. Warren, B. E. Newnam and J. C. Goldstein, IEEE J. Quantum Electron. **QE-21**, 882 (1985).
- ⁶J. Masud, T. C. Marshall, S. P. Schlesinger and F. G. Yee, Phys. Rev. Lett. **56**, 1567 (1986).
- ⁷J. Masud, T. C. Marshall, S. P. Schlesinger, F. G. Yee, W. M. Fawley E. T. Scharlemann, S. S. Yu, A. M. Sessler and E. J. Sternbach, Phys. Rev. Lett. **58**, 763 (1987).
- ⁸F. G. Yee, T. C. Marshall and S. P. Schlesinger, IEEE Trans. Plasma Sci. **PS-16**, 162 (1988).
- ⁹J. Fajans, G. Bekefi, Y. Z. Yin and B. Lax, Phys. Rev. Lett. **53**, 246 (1984).
- ¹⁰R. W. Warren, B. E. Newnam, J. G. Winston, W. E. Stein, L. M. Young and C. A. Brau, IEEE J. Quantum Electron. **QE-19**, 391 (1983).
- ¹¹G. Bekefi, R. E. Shefer and W. W. Destler, Appl. Phys. Lett. **44**, 280 (1983).
- ¹²C. W. Roberson, J. A. Pasour, F. Mako, R. F. Lucey, Jr. and P. Sprangle, Infrared Millimeter Waves **10**, 361 (1983), and references therein.
- ¹³A. Grossman, T. C. Marshall and S. P. Schlesinger, Phys. Fluids **26**, 337 (1983).
- ¹⁴D. Prosnitz and A. M. Sessler, In *Physics of Quantum Electronics* (Addison-Wesley, Reading, Massachusetts, 1982), Vol.9, p.651.

- ¹⁵R. K. Parker, R. H. Jackson, S. H. Gold, H. P. Freund, V. L. Granatstein, P. C. Efthimion, M. Herndon and A. K. Kinkead, *Phys. Rev. Lett.* **48**, 238 (1982).
- ¹⁶S. Benson, D. A. G. Deacon, J. N. Eckstein, J. M. J. Madey, K. Robinson, T. I. Smith and R. Taber, *Phys. Rev. Lett.*, **48A**, 235 (1982).
- ¹⁷A. N. Didenko, A. R. Borisov, G. R. Fomenko, A. V. Kosevnikov, G. V. Melnikov, Yu G. Stein and A. G. Zerlitsin, *IEEE Trans. Nucl. Sci.* **NS-28**, 3169 (1981).
- ¹⁸D. B. McDermott, T. C. Marshall, S. P. Schlesinger, R. K. Parker and V. L. Granatstein, *Phys. Rev. Lett.* **41**, 1368 (1978).
- ¹⁹D. A. G. Deacon, L. R. Elias, J. M. J. Madey, G. J. Ramian, H. A. Schwettman and T. I. Smith, *Phys. Rev. Lett.* **38**, 892 (1977).
- ²⁰L. R. Elias, W. M. Fairbank, J. M. J. Madey, H. A. Schwettman and T. I. Smith, *Phys. Rev. Lett.* **36**, 717 (1976).
- ²¹R. C. Davidson, *Phys. Fluids* **29**, 2689 (1986).
- ²²R. C. Davidson, J. S. Wurtele, and R. E. Aamodt, *Phys. Rev. A* **34**, 3063 (1986).
- ²³B. Lane and R. C. Davidson, *Phys. Rev. A* **27**, 2008 (1983).
- ²⁴R. C. Davidson and J. S. Wurtele, *Phys. Fluids* **30**, 557 (1987).
- ²⁵R. C. Davidson and J. S. Wurtele, *Phys. Fluids* **30**, 2825 (1987).
- ²⁶S. Riyopoulos and C. M. Tang, *Phys. Fluids* **31**, 1708 (1988).
- ²⁷S. Riyopoulos and C. M. Tang, *Phys. Fluids* **31**, 3387 (1988).
- ²⁸W. M. Sharp and S. S. Yu, *Phys. Fluids* **B2**, 581 (1990).
- ²⁹A. M. Dimos and R. C. Davidson, *Phys. Fluids* **28**, 677 (1985).
- ³⁰R. C. Davidson and Y. Z. Yin, *Phys. Fluids* **28**, 2524 (1985).
- ³¹T. Taguchi, K. Mima and T. Mochizuki, *Phys. Rev. Lett.* **46**, 824 (1981).
- ³²F. A. Hopf, P. Meystre, M. O. Scully and W. H. Louisell, *Phys. Rev. Lett.* **37**, 1342 (1976).
- ³³R. C. Davidson and W. A. McMullin, *Phys. Rev. A* **26**, 410 (1982).

- ³⁴N. S. Ginzburg and M. A. Shapiro, *Opt. Commun.* **40**, 215 (1982).
- ³⁵J. C. Goldstein and W. B. Colson, in *Proceedings of the International Conference on Lasers* (STS, McLean, VA, 1982), p.218.
- ³⁶W. B. Colson, *IEEE J. Quantum Electron.* **QE-17**, 1417 (1981).
- ³⁷P. Sprangle, C. M. Tang and W. M. Manheimer, *Phys. Rev. A* **21**, 302 (1980).
- ³⁸W. H. Louisell, J. F. Lam, D. A. Copeland and W. B. Colson, *Phys. Rev. A* **19**, 288 (1979).
- ³⁹N. M. Kroll, P. L. Morton and M. N. Rosenbluth, *IEEE J. Quantum Electron.* **QE-17**, 1436 (1981).
- ⁴⁰D. C. Quimby, J. M. Slater and J. P. Wilcoxon, *IEEE J. Quantum Electron.* **QE-21**, 979 (1985).
- ⁴¹N. S. Ginzburg and M. I. Petelin, *Int. J. Electron.* **59**, 291 (1985).
- ⁴²C. M. Tang and P. Sprangle, in *Free Electron Generators of Coherent Radiation*, Edited by C. A. Brau, S. F. Jacobs and M. O. Scully (Society of Optical Engineering, Bellingham, WA, 1983), Vol.453, p.11.
- ⁴³G. Dattoli, A. Marino, A. Renieri and F. Romanelli, *IEEE J. Quantum Electron.* **QE-17**, 1371 (1981).
- ⁴⁴W. B. Colson, in *Proceedings of the Seventh International Conference on Free Electron Lasers*, edited by E. T. Scharlemann and D. Prosnitz (North-Holland, Amsterdam, 1986), p.168.
- ⁴⁵M. N. Rosenbluth, H. V. Wong and B. N. Moore, in Ref.42, p.25.
- ⁴⁶A. T. Lin, *Phys. Quantum Electron.* **9**, 867 (1982).
- ⁴⁷H. Al-Abawi, J. K. McIver, G. T. Moore and M. O. Scully, *Phys. Quantum Electron.* **8**, 415 (1982).
- ⁴⁸W. B. Colson, *Phys. Quantum Electron.* **8**, 457 (1982).
- ⁴⁹J. Goldstein, in Ref.42, p.2.
- ⁵⁰R. C. Davidson and Y. Z. Yin, *Phys. Rev. A* **30**, 3078 (1984).

- ⁵¹G. L. Johnston and R. C. Davidson, *J. Appl. Phys.* **55**, 1285 (1984).
- ⁵²H. P. Freund and A. K. Ganguly, *Phys. Rev. A* **28**, 3438 (1983).
- ⁵³H. S. Uhm and R. C. Davidson, *Phys. Fluids* **26**, 288 (1983).
- ⁵⁴R. C. Davidson and H. S. Uhm, *J. Appl. Phys.* **53**, 2910 (1982).
- ⁵⁵H. S. Uhm and R. C. Davidson, *Phys. Fluids* **24**, 2348 (1981).
- ⁵⁶R. C. Davidson, W. A. McMullin and K. Tsang, *Phys. Fluids* **27**, 233 (1983).
- ⁵⁷R. C. Davidson and W. A. McMullin, *Phys. Fluids* **26**, 840 (1983).
- ⁵⁸W. A. McMullin and G. Bekefi, *Phys. Rev. A* **25**, 1826 (1982).
- ⁵⁹R. C. Davidson and W. A. McMullin, *Phys. Rev. A* **26**, 1997 (1982).
- ⁶⁰W. A. McMullin and G. Bekefi, *Appl. Phys. Lett.* **39**, 845 (1981).
- ⁶¹R. C. Davidson, *Phys. Fluids* **29**, 267 (1986).
- ⁶²R. C. Davidson and J. S. Wurtele, *IEEE Trans. Plasma Sci.* **PS-13**, 464 (1985).
- ⁶³H. P. Freund, R. A. Kehs and V. L. Granatstein, *IEEE J. Quantum Electron.* **QE-21**, 1080 (1985).
- ⁶⁴H. P. Freund and A. K. Ganguly, *IEEE J. Quantum Electron.* **QE-21**, 1073 (1985).
- ⁶⁵B. Hafizi and R. E. Aamodt, *Phys. Rev. A* **29**, 2656 (1984).
- ⁶⁶P. Sprangle, C. M. Tang and I. Bernstein, *Phys. Rev. A* **28**, 2300 (1983).
- ⁶⁷H. P. Freund and P. Sprangle, *Phys. Rev. A* **28**, 1835 (1983).
- ⁶⁸R. C. Davidson and H. S. Uhm, *Phys. Fluids* **23**, 2076 (1980).
- ⁶⁹P. Sprangle and R. A. Smith, *Phys. Rev. A* **21**, 293 (1980).
- ⁷⁰I. B. Bernstein and J. L. Hirshfield, *Physica (Utrecht) A* **20**, 1661 (1979).
- ⁷¹T. Kwan and J. M. Dawson, *Phys. Fluids* **22**, 1089 (1979).
- ⁷²T. Kwan, J. M. Dawson and A. T. Lin, *Phys. Fluids* **20**, 581 (1977).

- ⁷³A. Bambini and A. Renieri, *Nuovo Cimeto Lett.* **21**, 399 (1978).
- ⁷⁴S. T. Stenholm and A. Bambini, *IEEE J. Quantum Electron.* **QE-17**, 1363 (1981).
- ⁷⁵C. W. Roberson and P. Sprangle, *Phys. Fluids* **B1**, 3 (1989).
- ⁷⁶R. C. Davidson, *Physics of Nonneutral Plasmas* (Addison-Wesley, Reading, Massachusetts, 1990), Chapter 7.
- ⁷⁷N. M. Kroll and W. A. McMullin, *Phys. Rev. A* **17**, 300 (1978).
- ⁷⁸A. Hasegawa, *Bell Syst. Tech. J.* **57**, 3069 (1978).
- ⁷⁹W. B. Colson, *Phys. Lett. A* **59**, 187 (1976).
- ⁸⁰V. P. Sukhatme and P. A. Wolff, *J. Appl. Phys.* **44**, 2331 (1973).
- ⁸¹R. C. Davidson, *Phys. Lett. A* **126**, 21 (1987).
- ⁸²R. C. Davidson, T.-Y. Yang and R. E. Aamodt, *J. Plasma Phys.* **41**, 405 (1989).
- ⁸³G. L. Johnston, F. Hartemann, R. C. Davidson and G. Bekefi, *Phys. Rev. A* **38**, 1309 (1988).
- ⁸⁴T.-Y. B. Yang and R. C. Davidson, (submitted to *The Physics of Fluids*).
- ⁸⁵I. B. Bernstein and S. K. Trehan, *Nucl. Fusion* **1**, 3 (1960); see also pp. 21-23.
- ⁸⁶R. C. Davidson, in *Handbook of Plasma Physics*, edited by A. A. Galeev and R. N. Sudan (North-Holland, New York, 1983), Vol. 1, pp. 521-585; see also pp. 546 and 547.
- ⁸⁷T. H. Stix, *The Theory of Plasma Waves* (McGraw-Hill, New York, 1962).
- ⁸⁸J. D. Jackson, *Classical Electrodynamics* (John Wiley & Sons, New York, 1975), chapter 11.

FIGURE CAPTIONS

Fig.1 In the equilibrium state ($\partial/\partial t' = 0$), electron motion in the phase space (z', p'_z) occurs on surfaces with $\gamma' = \text{const.}$

Fig.2 Plots of the normalized growth rate $\text{Im}(\Delta\Omega')/\Omega'_B$ versus normalized wavenumber $\Delta K'/\Omega'_B$ obtained from Eq. (89) for the choices of pump parameter corresponding to (a) $(\Omega'_B/\Gamma'_0)^6/4 = 10^3$, (b) $(\Omega'_B/\Gamma'_0)^6/4 = 1.0$ and (c) $(\Omega'_B/\Gamma'_0)^6/4 = 10^{-3}$.

Fig.3 Time evolution of the fastest growing sideband mode with $\Delta K' = \Delta K'_M = 10^{-2}$ for the choice of system parameters $\epsilon'_p = 3.1623 \times 10^{-7}$, $\epsilon'_w = 0.1$ and $\hat{a}_s^0 = 10^{-3}$ (Case I in Sec.V B). Shown here are plots of the Fourier amplitudes (a) $\delta A_{\Delta K'}^r/\hat{a}_s^0$, (b) $\delta A_{\Delta K'}^i/\hat{a}_s^0$ and $\delta\theta'_{\Delta K'}$ obtained from Eq. (109). The variables $\delta A_s(\xi', \tau')$ and $\delta\theta'_{s,\mu}(\tau')$ in Eq. (109) are obtained directly by solving Eqs. (101)-(103) for the case of small-amplitude initial conditions with wavenumber $\Delta K' = \Delta K'_M = 10^{-2}$.

Fig.4 Time evolution of the fastest growing sideband mode with $\Delta K' = \Delta K'_M = 10^{-2}$ for the choice of system parameters $\epsilon'_p = 5.807 \times 10^{-6}$, $\epsilon'_w = 3.37 \times 10^{-2}$ and $\hat{a}_s^0 = 10^{-3}$ (Case II in Sec.V B). Shown here are plots of the Fourier amplitudes (a) $\delta A_{\Delta K'}^r/\hat{a}_s^0$, (b) $\delta A_{\Delta K'}^i/\hat{a}_s^0$ and $\delta\theta'_{\Delta K'}$ obtained from Eq. (109). The variables $\delta A_s(\xi', \tau')$ and $\delta\theta'_{s,\mu}(\tau')$ in Eq. (109) are obtained directly by solving Eqs. (101)-(103) for the case of small-amplitude initial conditions with wavenumber $\Delta K' = \Delta K'_M = 10^{-2}$.

Fig.5 Time evolution of the fastest growing sideband mode with $\Delta K' = \Delta K'_M = 10^{-2}$ for the choice of system parameters $\epsilon'_p = 10^{-6}$, $\epsilon'_w = 10^{-3}$ and $\hat{a}_s^0 = 10^{-4}$ (Case III in Sec.V B). Shown here are plots of the Fourier amplitudes (a) $\delta A_{\Delta K'}^r/\hat{a}_s^0$, (b) $\delta A_{\Delta K'}^i/\hat{a}_s^0$ and $\delta\theta'_{\Delta K'}$ obtained from Eq. (109). The variables $\delta A_s(\xi', \tau')$ and $\delta\theta'_{s,\mu}(\tau')$ in Eq. (109) are obtained directly by solving Eqs. (101)-(103) for the case of small-amplitude initial conditions with wavenumber $\Delta K' = \Delta K'_M = 10^{-2}$.

Fig.6 Time evolution of the Fourier amplitudes $\delta A_{\Delta K'}^r$ and $\delta A_{\Delta K'}^i$ for Case I with the choice of system parameters $\epsilon'_p = 3.1623 \times 10^{-7}$, $\epsilon'_w = 0.1$ and $\hat{a}_s^0 = 10^{-3}$. Shown in (a) and (b) are the amplitudes of the sideband signals with wavenumber $\Delta K' = \Delta K'_M/2 = 5 \times 10^{-3}$. Shown in (c) and (d) are the amplitudes of the

sideband signals with wavenumber $\Delta K' = \Delta K'_M = 10^{-2}$. The initial conditions in this figure correspond to small-amplitude perturbations with wavenumber $\Delta K' = \Delta K'_M/2 = 5 \times 10^{-3}$.

Fig.7 Time evolution of the Fourier amplitudes $\delta A_{\Delta K'}^r$ and $\delta A_{\Delta K'}^i$ for Case II with the choice of system parameters $\epsilon'_p = 5.807 \times 10^{-6}$, $\epsilon'_w = 3.37 \times 10^{-2}$ and $\hat{a}_s^0 = 10^{-3}$. Shown in (a) and (b) are the amplitudes of the sideband signals with wavenumber $\Delta K' = \Delta K'_M/2 = 5 \times 10^{-3}$. Shown in (c) and (d) are the amplitudes of the sideband signals with wavenumber $\Delta K' = \Delta K'_M = 10^{-2}$. The initial conditions in this figure correspond to small-amplitude perturbations with wavenumber $\Delta K' = \Delta K'_M/2 = 5 \times 10^{-3}$.

Fig.8 Time evolution of the Fourier amplitudes $\delta A_{\Delta K'}^r$ and $\delta A_{\Delta K'}^i$ for Case III with the choice of system parameters $\epsilon'_p = 10^{-6}$, $\epsilon'_w = 10^{-3}$ and $\hat{a}_s^0 = 10^{-4}$. Shown in (a) and (b) are the amplitudes of the sideband signals with wavenumber $\Delta K' = \Delta K'_M/2 = 5 \times 10^{-3}$. Shown in (c) and (d) are the amplitudes of the sideband signals with wavenumber $\Delta K' = \Delta K'_M = 10^{-2}$. The initial conditions in this figure correspond to small-amplitude perturbations with wavenumber $\Delta K' = \Delta K'_M/2 = 5 \times 10^{-3}$.

Fig.9 Plots versus real wavenumber $\Delta K'$ of (a) the growth rate $\text{Im}(\Delta\Omega')$ and (b) the real frequency shift $\text{Re}(\Delta\Omega')$ obtained from the dispersion relation (89) for the choice of system parameters $\epsilon'_p = 5.6 \times 10^{-7}$, $\epsilon'_w = 0.48$ and $\hat{a}_s^0 = 2.4 \times 10^{-4}$ corresponding to the Los Alamos free electron laser.⁵

Fig.10 Time evolution of the sideband instability for the choice of system parameters $\epsilon'_p = 5.6 \times 10^{-7}$, $\epsilon'_w = 0.48$ and $\hat{a}_s^0 = 2.4 \times 10^{-4}$. The normalized power $P'_{\Delta K'}$ defined in Eq. (125) is plotted versus τ' for first six Fourier components, i.e., $\Delta K' = m/252$, $m = 1, \dots, 6$. The lower sidebands correspond to the solid curves, and the upper sidebands correspond to the dotted curves. The curves in Figs. 10-12 are obtained in the same numerical calculation.

Fig.11 Plots versus τ' of the real frequency shift $(-d\psi'_{\Delta K'}/d\tau' - \Delta K')$ [see the paragraph following Eqs. (114)-(116)] corresponding to the lower sideband signals for (a) $\Delta K' = 1/84$ and (b) $\Delta K' = 1/42$. The curves in Figs. 10-12 are obtained in the same numerical calculation.

Fig.12 Plots versus τ' of (a) the normalized power $A_p^2/(\hat{a}_s^0)^2$ for the primary signal

[see Eq. (116) and the paragraph following Eq. (116)] and (b) the normalized spatially averaged power $\langle \hat{a}_s^2 \rangle / (\hat{a}_s^0)^2$ defined in Eq. (126). The curves in Figs. 10-12 are obtained in the same numerical calculation.

Fig.13 Plots versus frequency shift $\Delta\omega/\omega_s$ of the relative power spectrum $P(\Delta\omega)$, which is proportional to the amplitude-squared of the Fourier transform of $a_s^-(z_0, t)$ defined in Eq. (112) at $z = z_0$ in the laboratory frame. Here, $a_s^-(z, t)$ is obtained from $a_s(z', t')$ calculated in Sec.V D. In obtaining the Fourier transform plot in (a), the data for the entire evolution from $\tau' = 0$ to $\tau' = 6000$ are used. In contrast, only the data from $\tau' = 4000$ to $\tau' = 6000$ are used to obtain the plot in (b).

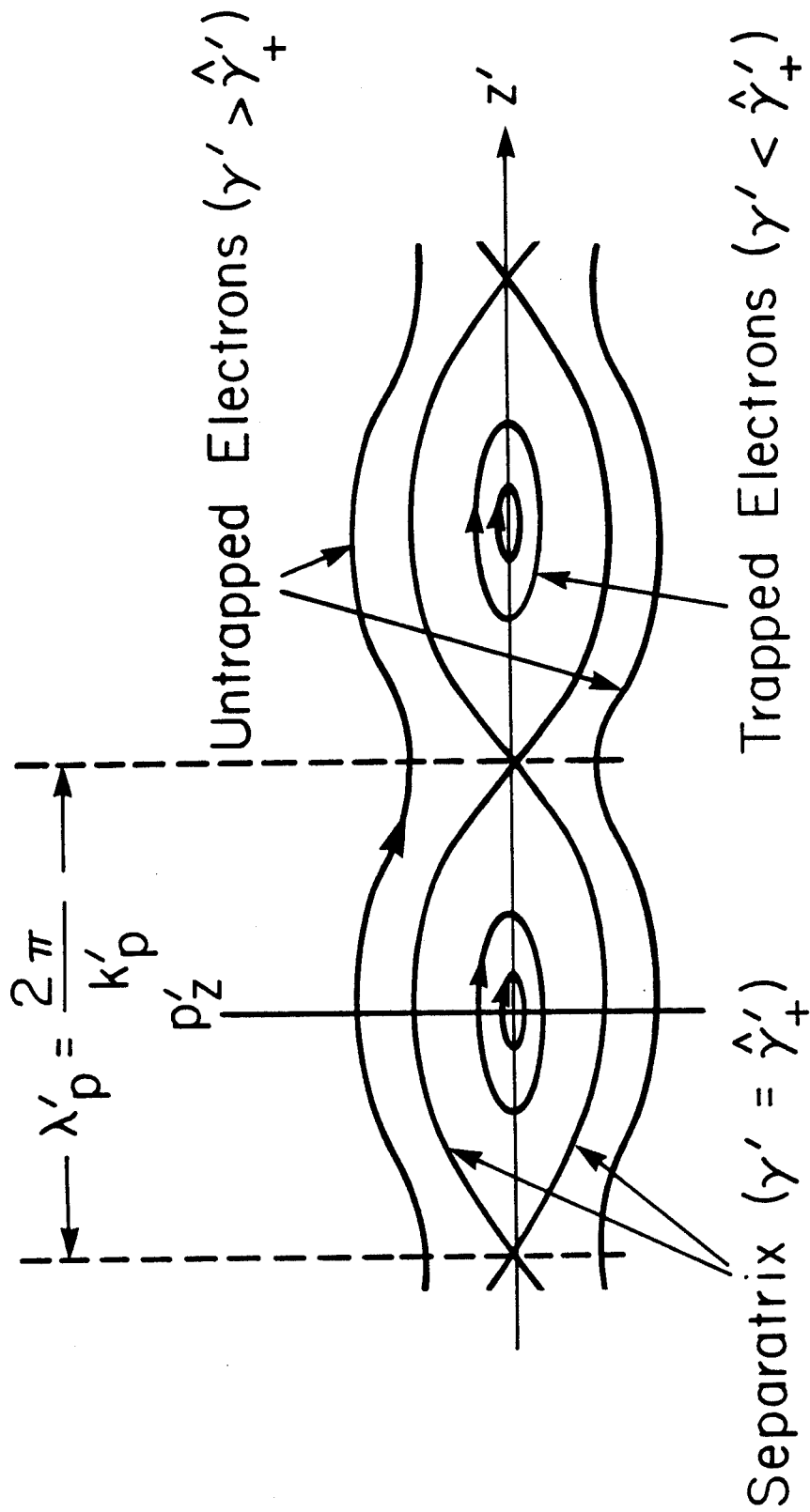


Fig. 1

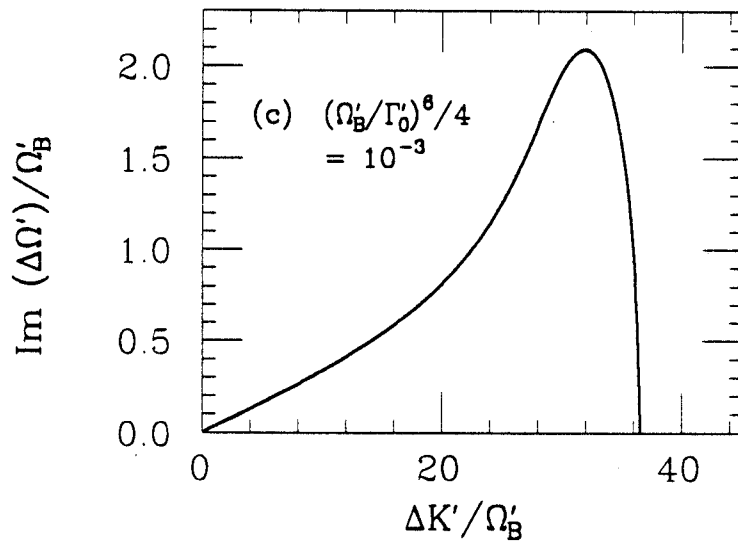
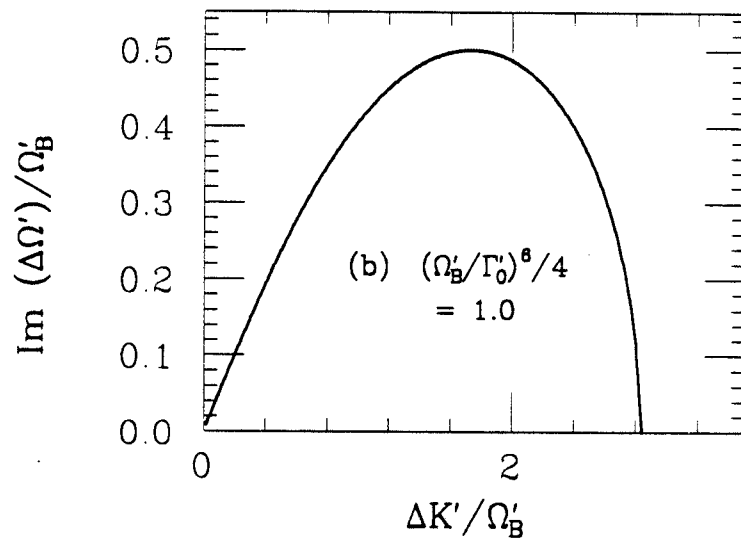
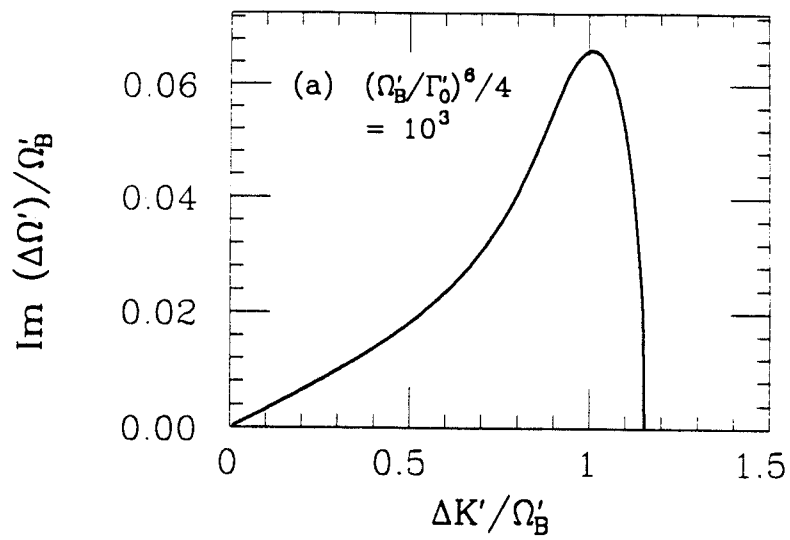


Fig. 2

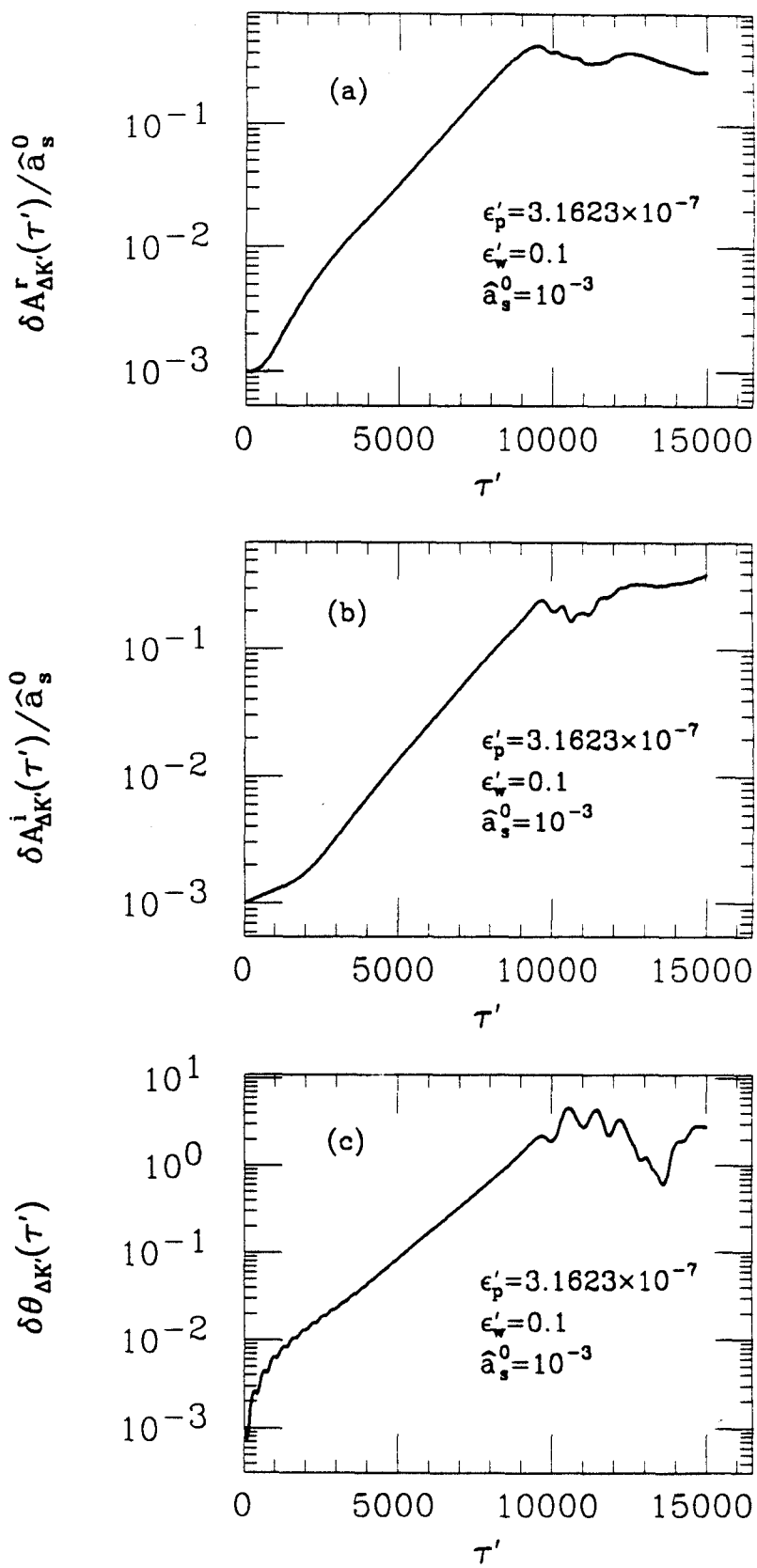


Fig. 3

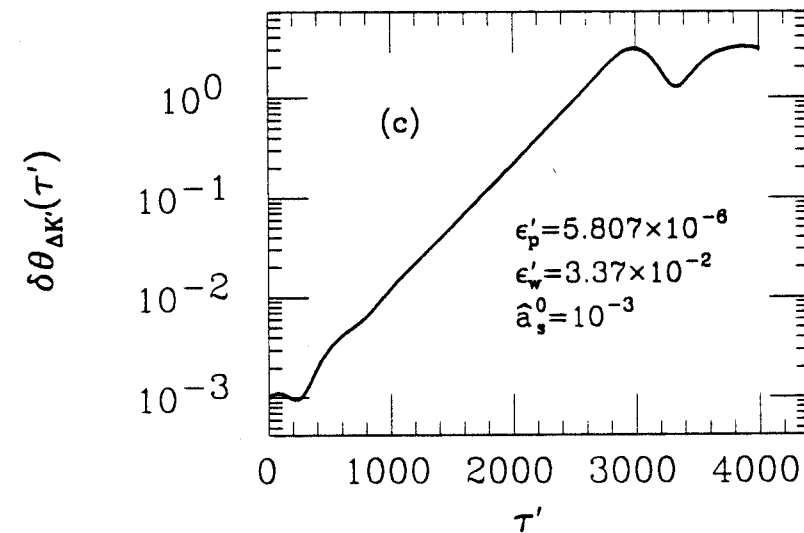
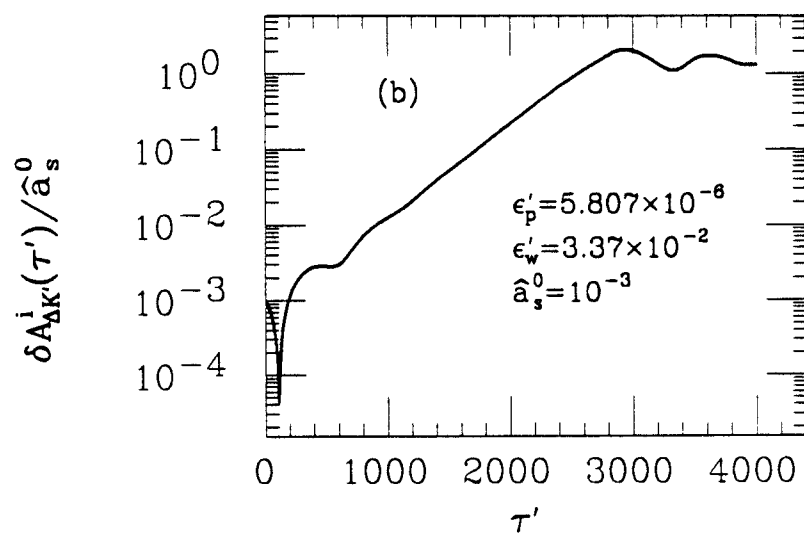
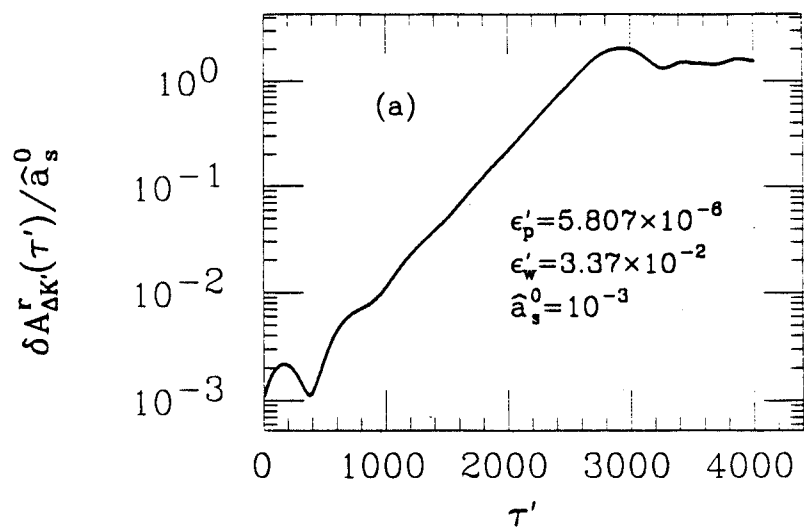


Fig. 4

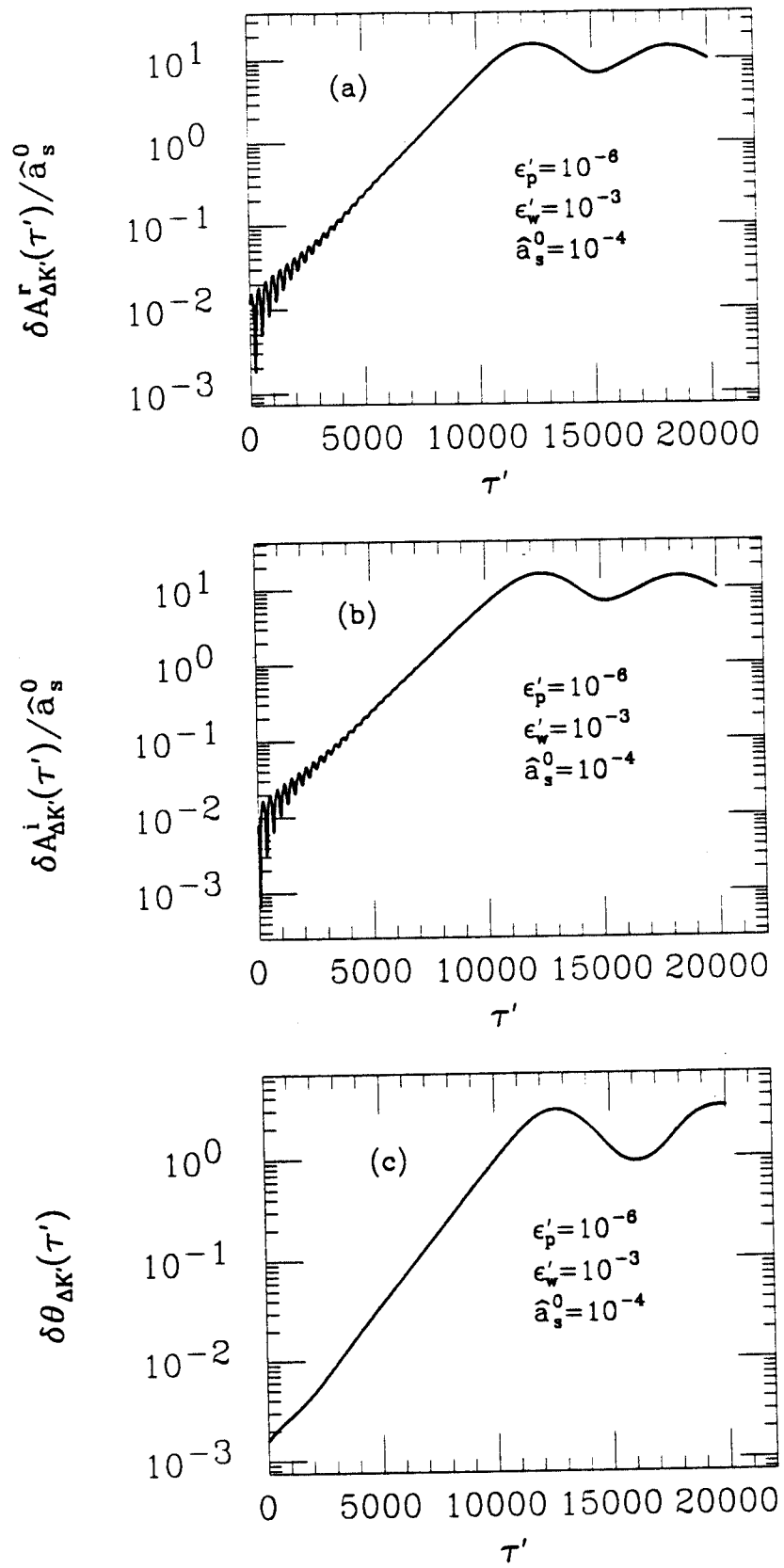


Fig. 5

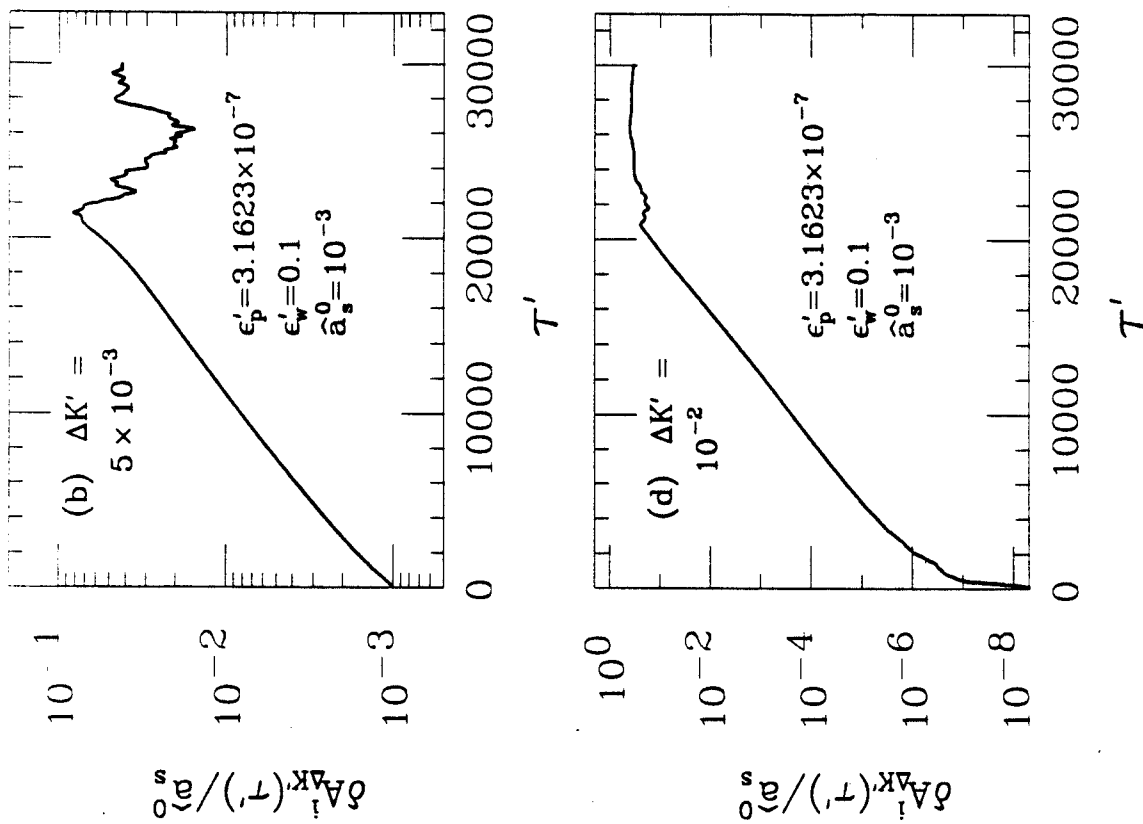


Fig. 6

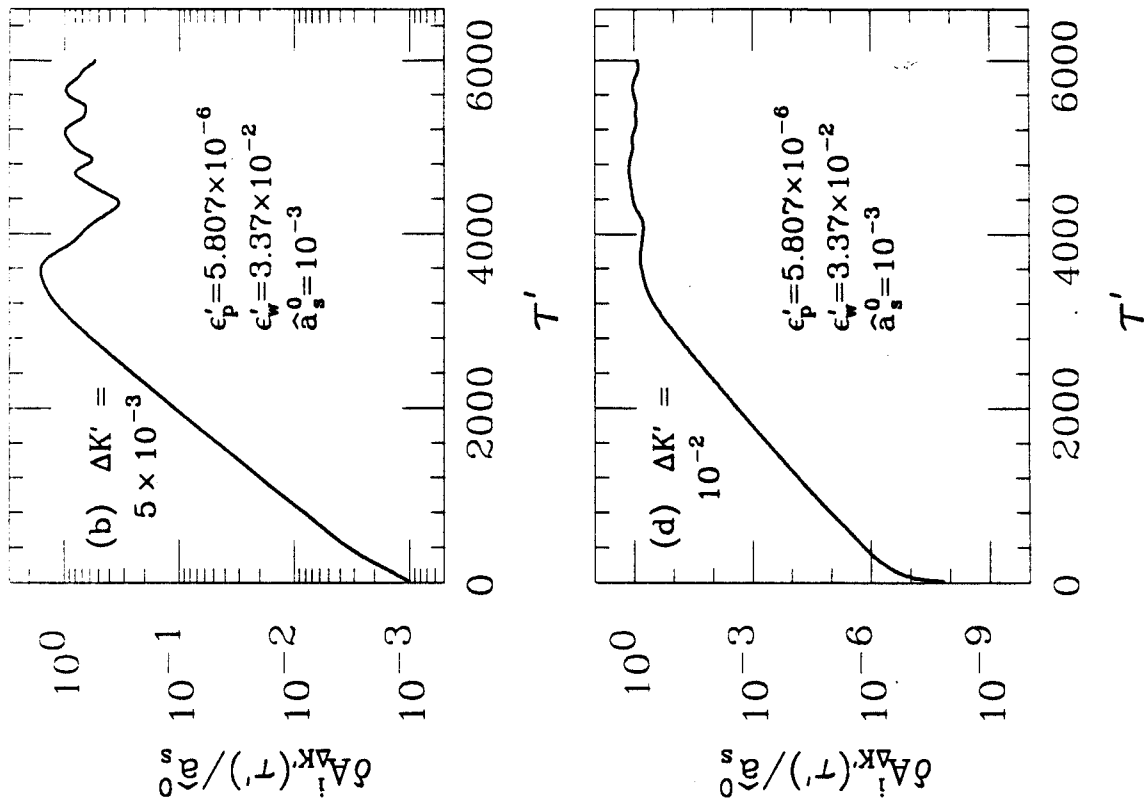


Fig. 7

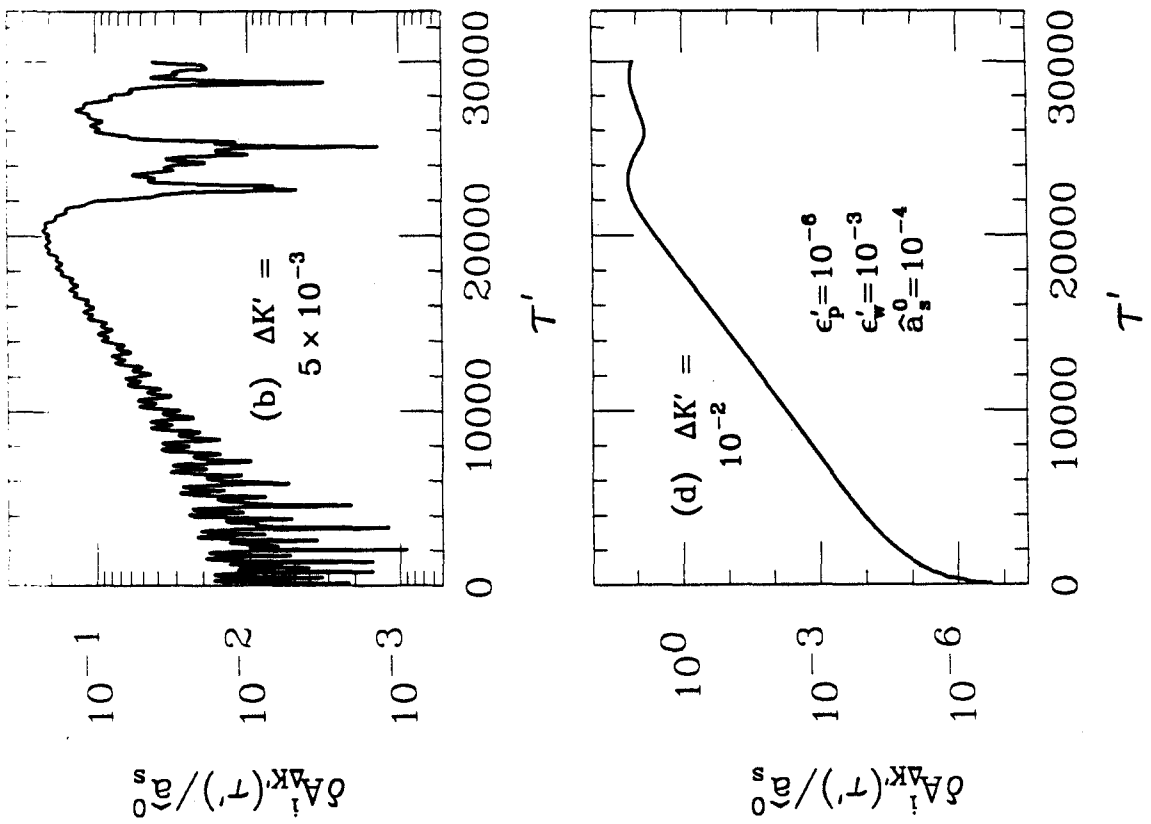


Fig. 8

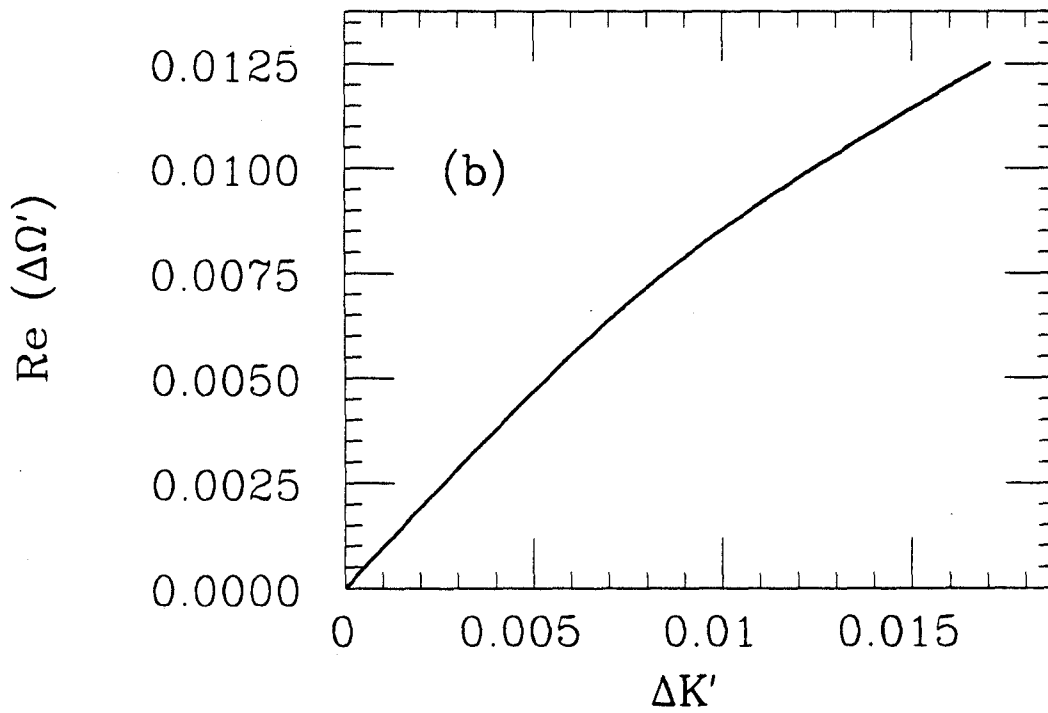
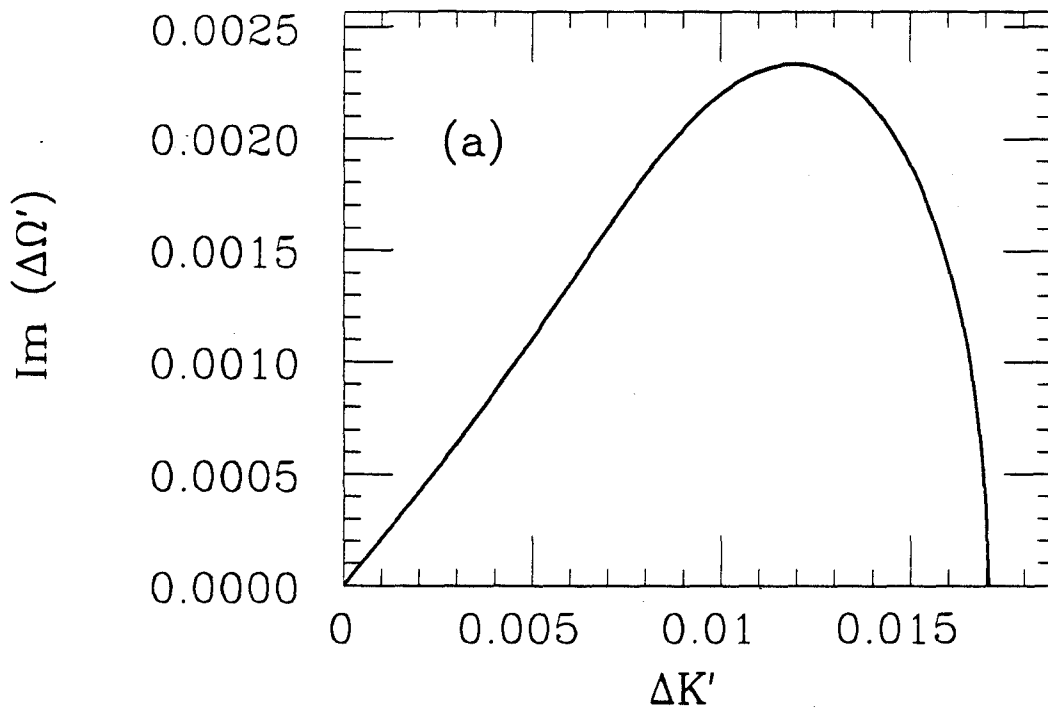


Fig. 9

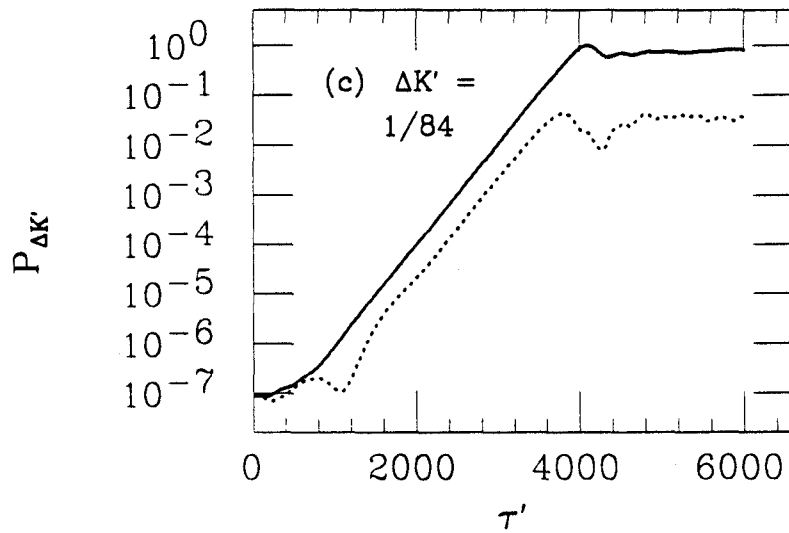
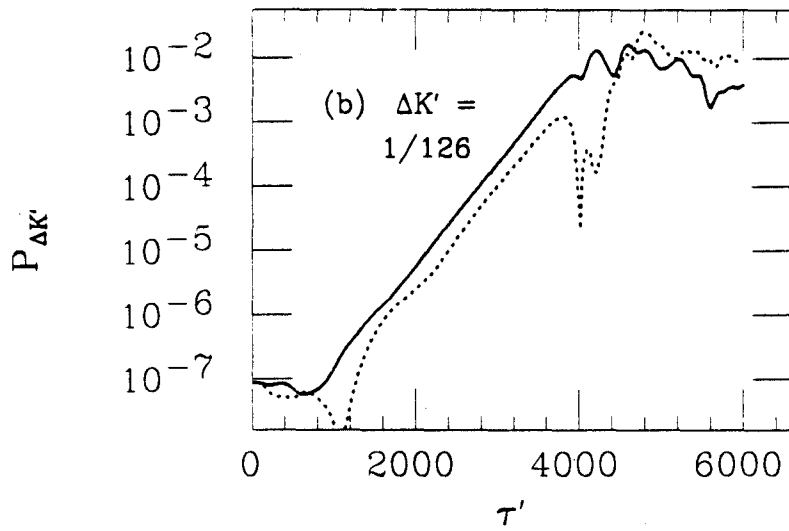
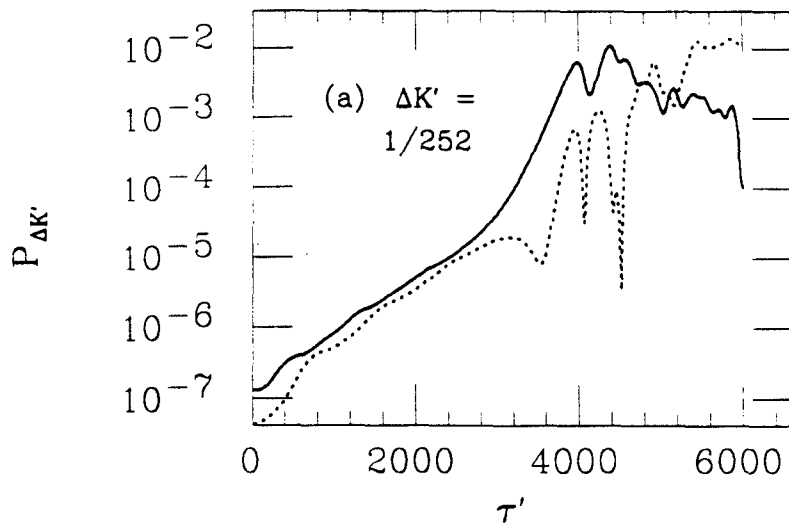
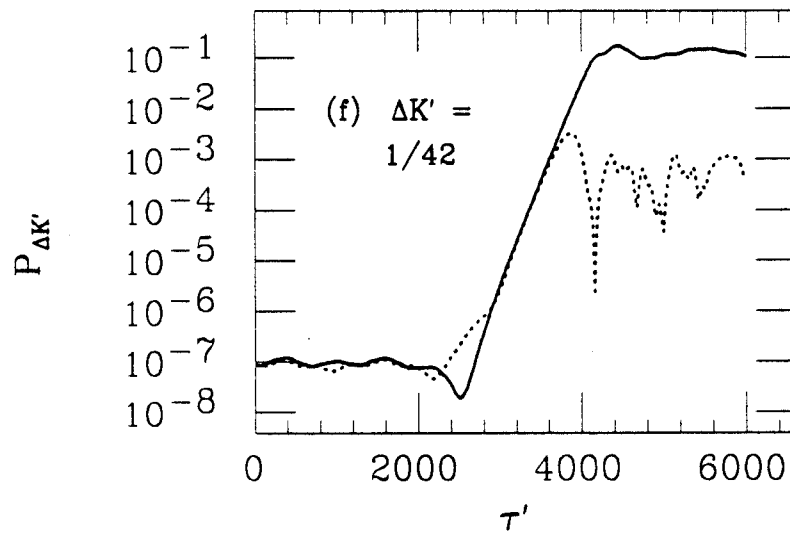
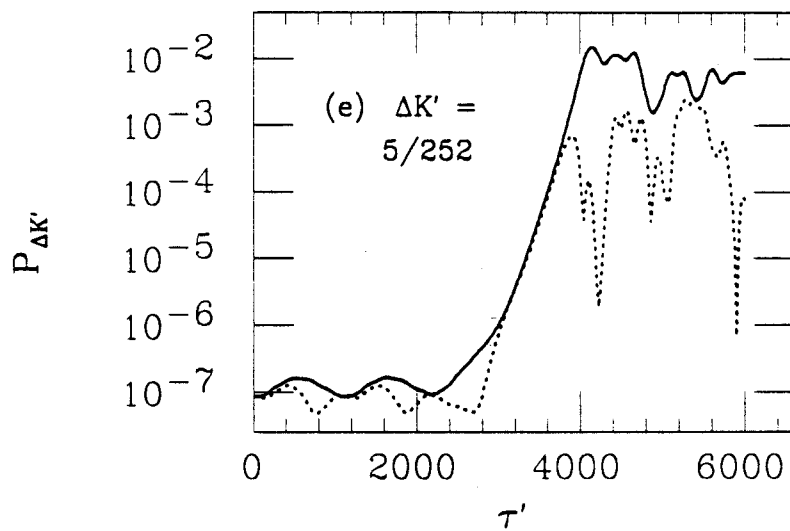
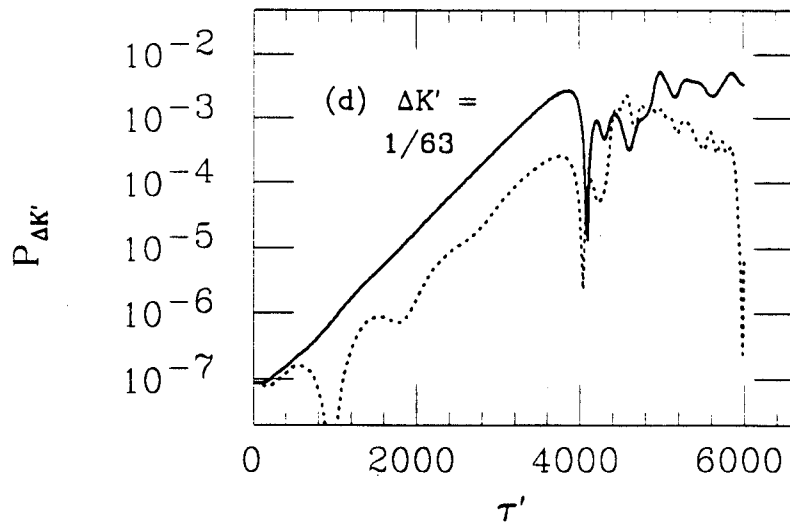


Fig. 10(a) - 10(c)



Figs. 10(d) - 10(f)

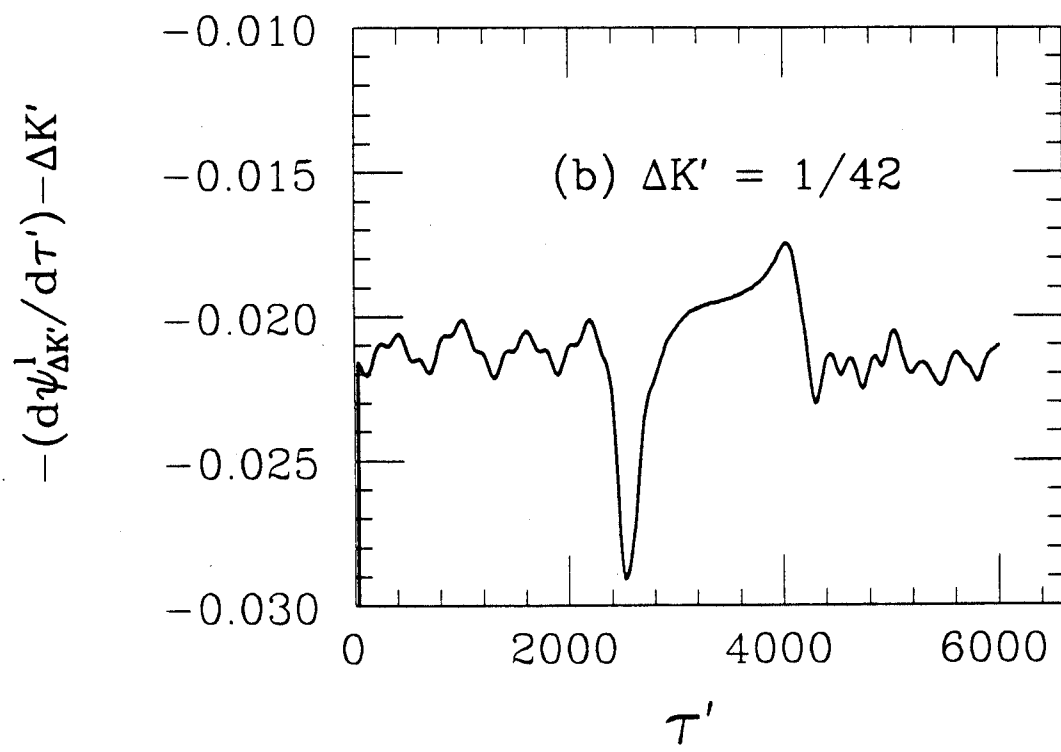
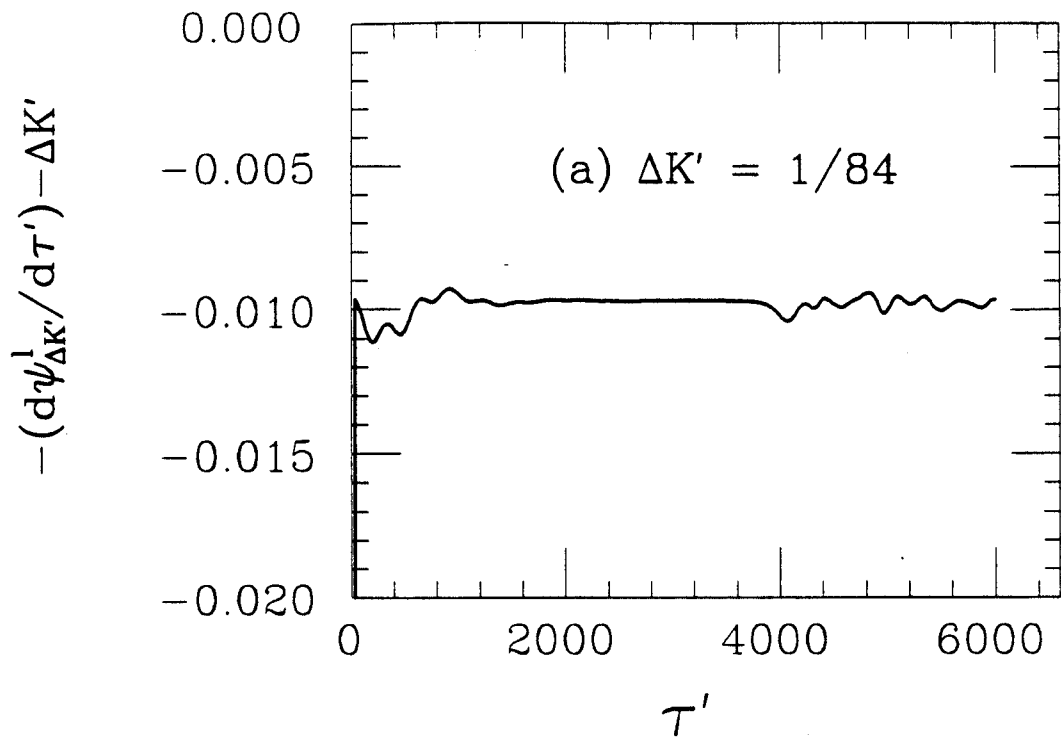


Fig. 11

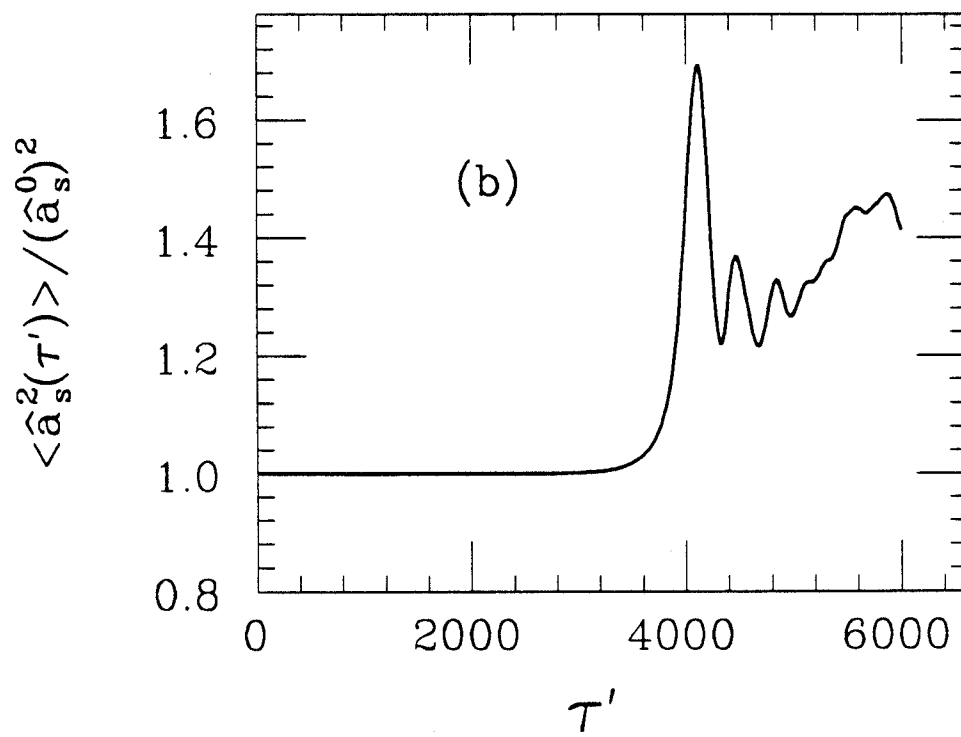
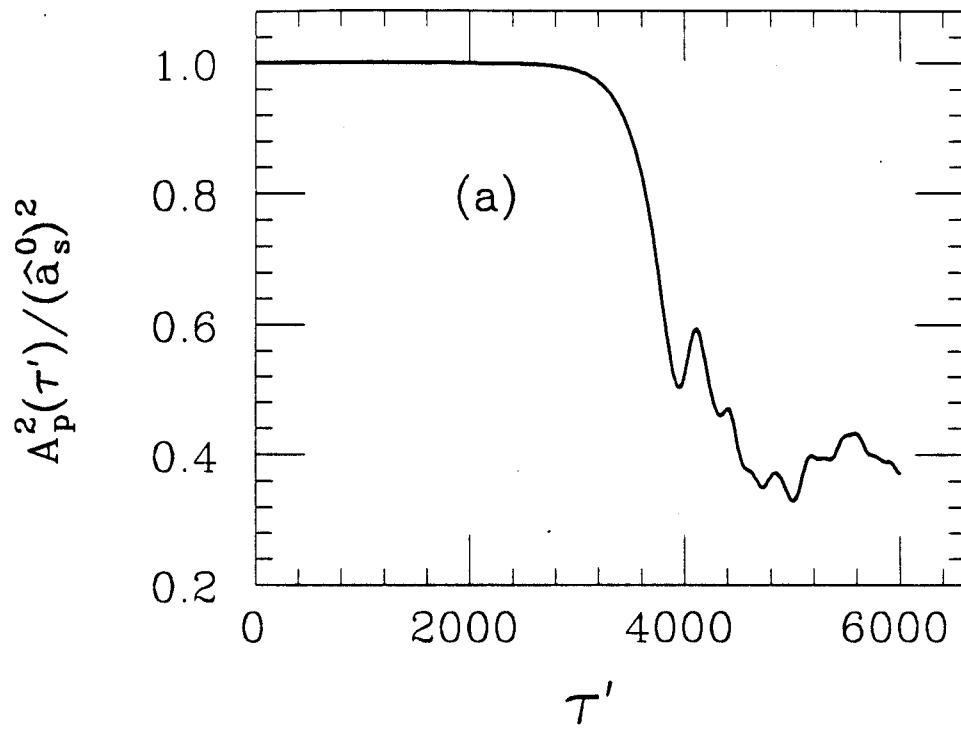


Fig. 12

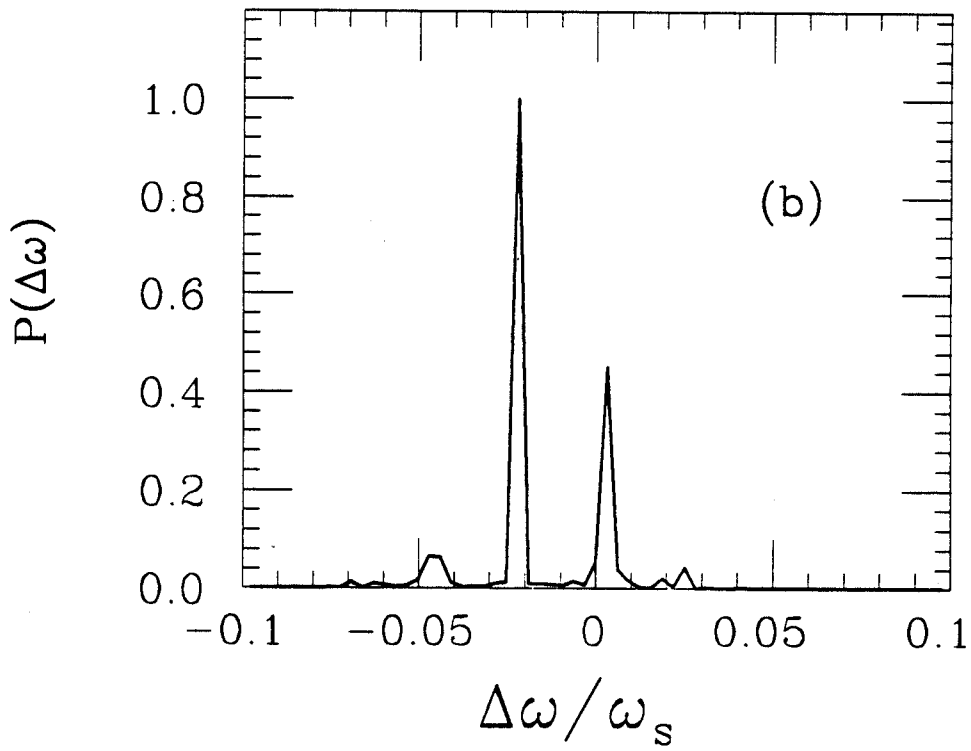
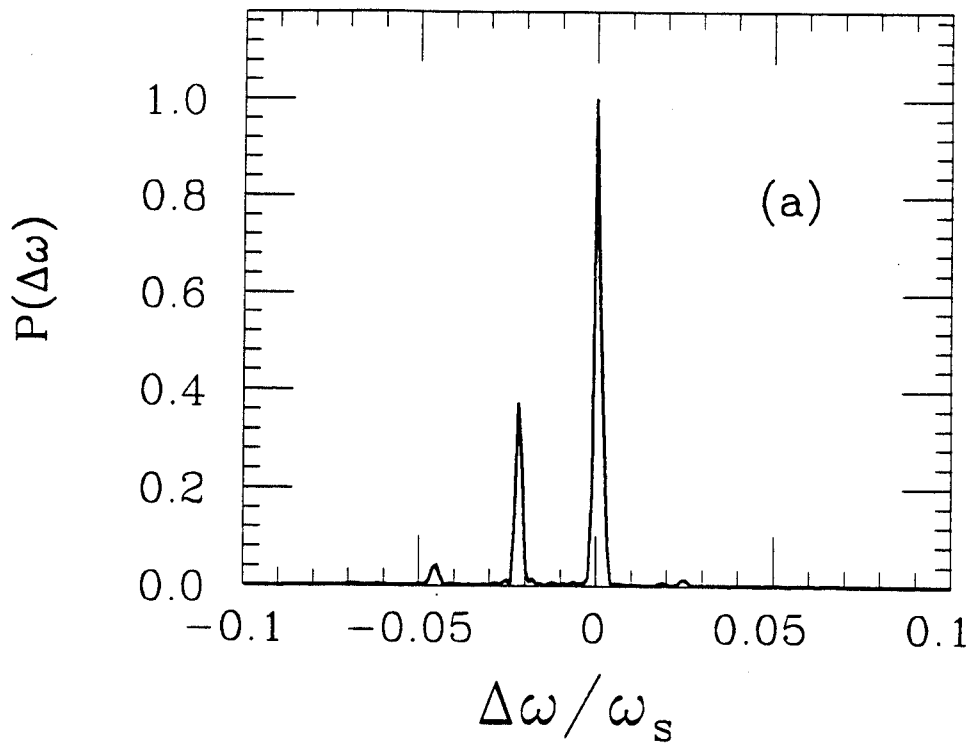


Fig. 13

